Contents lists available at ScienceDirect

Comput. Methods Appl. Mech. Engrg.

journal homepage: www.elsevier.com/locate/cma

Volume conservation issue within SPH models for long-time simulations of violent free-surface flows

C. Pilloton [a], P.N. Sun [b], X. Zhang [b], A. Colagrossi [a,c,*]

[a] CNR-INM, Institute of Marine Engineering, Via di Vallerano 139, 00128 Roma, Italy
[b] School of Ocean Engineering and Technology, Sun Yat-sen University, Zhuhai, 519000, China
[c] École Centrale Nantes, LHEEA Lab. (ECN/CNRS), Nantes, France

ARTICLE INFO

ABSTRACT

Smoothed Particle Hydrodynamics (SPH) simulations of violent sloshing flows characterized by a strong fragmentation of free-surface can be affected by volume conservation errors. These errors can accumulate in time and preclude the possibility of using such models for long-time simulations. In the present work, different techniques to measure directly the particles' volumes by their positions are displayed. Thanks to these algorithms, we discussed how volume errors develop when introducing stabilization terms in the standard SPH schemes. Further, we show that the control of these errors can be achieved through two different (non-alternative) stabilization terms: (i) enforcement of dynamic boundary conditions on thin fluid jets and drops; and (ii) a dynamical switch that can impose or not the time variation of the particle masses.

To demonstrate the effectiveness of the numerical techniques, four different violent sloshing flows are investigated and compared with experimental data.

1. Introduction

After more than twenty years of rapid development, Smoothed Particle Hydrodynamics model has become widely used for solving hydrodynamic problems characterized by violent free-surface flows (see *e.g.* [1–7]).

In particular, in the weakly-compressible SPH models (see *e.g.* [8]), the particle evolution equations can be integrated in time through an explicit method. This method can be easily coded to run on massively parallel computers and/or Graphics Processing Units (GPUs). For this reason, these SPH models are widely applied in different engineering fields making it possible to run high-fidelity simulations with a wide number of particles (see *e.g.* [9–13]).

In the previous literature, there are many studies focusing on improving the accuracy, efficiency and stability of the SPH scheme. However, there are very few studies focusing on volume conservation issues. In violent free-surface flow simulations where the liquid interfaces are highly fragmented, volume errors can occur and accumulate in time. In the literature researchers have mainly focused on weakly compressible SPH models and simulations; however volume error is also an important issue for the incompressible SPH model as discussed in [14–16] and generally for other particle methods [17].

In the original form of the SPH, based on the compressible flows model and born for solving astrophysical problems (see *e.g.* [18]), the "geometrical volumes" $\mathcal{V}_i$ of the generic particle ith are a direct function of the particle positions $\boldsymbol{r}_i$. In fact, the particles carry their own masses m_i which does not change in time, the density and the geometrical volume of the particles are evaluated by:

$$\rho_i(t) = \sum_j m_j\, W(\boldsymbol{r}_i, \boldsymbol{r}_j), \qquad \mathcal{V}_i(t) = \frac{m_i}{\rho_i(t)} = \frac{m_i}{\sum_j\, m_j\, W(\boldsymbol{r}_i, \boldsymbol{r}_j)}, \tag{1}$$

where W is a kernel function (see Section 2.2) which depends only by the particle positions. As a consequence, the conservation of the mass is ensured and the volume variations are strictly related to the compressibility of the media.

When considering weakly-compressible free-surface flows as in the pioneering work by Monaghan [19], to overcome the problem of the truncation of the kernel support close to the free-surface, the density ρ_i can be evaluated by integrating in time the continuity equations. In the following, such a scheme will be called "Standard SPH". In this scheme, the masses of the particles are still constant while the SPH particle volumes are evaluated with $V_i = m_i/\rho_i$. As a consequence, because of the errors in the time integration of the continuity equation, the volumes of the particles are not more directly linked to the particle positions. Therefore, local discrepancies between the geometrical volume $\mathcal{V}_i$ and the SPH one V_i can appear, as further discussed and shown in this work.

It is well known that the standard SPH model suffers from instability over the pressure field, which can be controlled by adding numerical diffusion into the scheme. The first attempt was done by Colagrossi and Landrini [20] who periodically filtered the density of the particles during the time evolution. An alternative approach was proposed by Vila and Ben Moussa [21,22] through the use of SPH schemes based on Riemann solvers, which approximate the fluxes of conservative variables through the particles. The use of Riemann solvers involves the addition of numerical diffusion in both continuity and momentum equations, stabilizing the pressure field and filtering out spurious numerical high-frequency noise (see *e.g.* [23]). A simplified version of the above Riemann-SPH models is the δ-SPH, where an explicit diffusive term is directly added into the continuity equation [24,25]. The δ-SPH model was successfully applied to several hydrodynamics problems, proving to be accurate and robust, and it became one of the most popular SPH variants.

The above corrected SPH models are designed to conserve the total mass but errors in volume conservation are worse than the standard SPH scheme. The reason is linked to the numerical diffusion added in the continuity equation, which introduces secular terms between the SPH total volume $V = \sum_i V_i$ and the geometrical one $\mathcal{V} = \sum_i \mathcal{V}_i$. The secular terms arise from the fact that diffusion correction acts with a constant sign. A theoretical analysis of this aspect is not the focus of the present work and, being it not trivial, it is left for future works. The aim of this work is to declare the presence of this drift on the volume error over time and show its measurement and a possible solution to control it.

In the more recent SPH models, in addition to numerical diffusive terms, the use of Particle Shifting Techniques (PSTs) is becoming more widespread (see *e.g.* [26–29]). Thanks to PST it is possible to regularize particles' spatial displacements, improving the accuracy of the method. However, as emphasized by Sun et al. [29] and recently by Khayyer et al. [30], also PST leads to secular terms on the time behaviour of the volume errors, especially for long-time and violent flow simulations. In recent works by Lyu & Sun [31] and Gao & Fu [32], it was shown that PST can be designed in order to control the volume error. In contrast, in Sang-Yoo et al. [33], an Arbitrarily-Lagrangian–Eulerian SPH (ALE-SPH) model is investigated for studying sloshing flows, revealing some advantages on the volume conservation due to the possibility of changing the particle masses and volumes consistently at run-time.

With respect to the test-cases used in [31–33] the problems discussed in the present work are characterized by more violent flows with longer time evolution. Moreover, in some of the test-cases the surface tension effect cannot be neglected and it is shown how it plays a relevant role in reducing the accumulation of volume errors. The challenging test-cases presented here can be adopted by the SPH community as special benchmarks for controlling the volume conservation of the specific SPH model adopted.

The present article is organized as follows:

(i) In Section 2 five different SPH models adopted are introduced with the new corrections proposed for controlling the volume errors during the time evolution;
(ii) In Section 3 two techniques to measure the fluid volume error in SPH simulations are proposed;
(iii) In Section 4 four selected benchmarks of violent sloshing flows are described with brief notes on the related experimental set-up;
(iv) In Section 5, numerical results obtained with the five different SPH models of the four different test-cases are presented underlying the effect of both viscosity and surface tension on the accumulation of volume errors.

2. SPH models with proposed techniques to control the total volume

In this section, the initialization of the SPH simulations is discussed, along with a brief introduction to the SPH models used for the present investigation. A possible technique for controlling the volume errors is also discussed. In the following, it is considered a fluid domain occupied by a liquid which is modelled as a weakly-compressible media (with variations of density field that are confined within 1%).

2.1. Initial setting and evaluation of the particle volumes and masses

The fluid domain is discretized in particles that are set initially on a lattice with homogeneous spacing Δr. It follows that the initial particles' volumes V_{i0}, at time $t = t_0 = 0$, are evaluated as $V_{i0} = \Delta r^n$ where n is the number of spatial dimensions. In the present work, all the particles have the same size, therefore, the total volume of the discretized fluid domain, V_0, is equal to $V_0 = N_{part} V_{i0}$. The initial particle masses m_{0i} are calculated through the prescribed initial density field, *i.e.* $m_{0i} = \rho_{0i} V_{0i}$ and the initial total mass of the liquid is $M_0 = \sum_i m_{0i}$.

Depending on the specific SPH model adopted, the particle masses m_i may or may not be constant during the time evolution. The particle densities ρ_i are always evaluated through the time integration of a continuity equation. Even if the mass of the particles changes over time, all the SPH models adopted in the present work preserve the total mass of the system, *i.e.*

$$\sum_i m_i(t) = M_0 \qquad \forall t \in [t_0, t_{end}],$$

where t_{end} is the last time instant of the simulation at hand. During the time evolution, the SPH volumes V_i are evaluated directly as $V_i = m_i/\rho_i$ which are not directly linked with the particle positions and they cannot be used to evaluate geometrical volumes. It follows that errors on the geometrical volumes $\mathcal{V}_i$ can accumulate during the time integration of the particle evolution equations. As a consequence the total volume of the particle system is not preserved, hence, the error has to be monitored through time evolution:

$$\epsilon_V(t) := \frac{\mathcal{V}(t) - V_0}{V_0}, \qquad \mathcal{V} = \sum_i \mathcal{V}_i, \tag{2}$$

where $\mathcal{V}$ is the geometric volume occupied by the whole set of SPH particles.

It is important to emphasize that the geometric volume $\mathcal{V}$ is not equal to the sum of the SPH volumes $\sum_i V_i$. This is a key point for the SPH models and it is particularly true when the SPH continuity equation contains diffusive terms added for improving the stability and the accuracy of the schemes and/or a PST is adopted. Obviously, the geometric volume $\mathcal{V}$ is strictly related to the particle positions and in Section 3 two different algorithms are proposed to evaluate this quantity.

The SPH volumes V_i, being directly linked with the density field, always respect the weakly compressible constraint, hence, the sum $\sum_i V_i$ remains always bounded within the 1% variation with respect to the initial total volume V_0. This is not the case for ϵ_V, as shown in the next sections, this error without any control can become in time higher than 1%.

2.2. Discrete SPH equations

Following the work by Antuono et al. [34], the Navier–Stokes equations for compressible fluids can be discretized within the δ-ALE-SPH scheme as follows:

$$\begin{cases} \dfrac{d\rho_i}{dt} = -\rho_i \sum_j (\boldsymbol{u}_{ji} + \delta\boldsymbol{u}_{ji}) \cdot \nabla_i W_{ij} V_j + \sum_j (\rho_j \delta\boldsymbol{u}_j + \rho_i \delta\boldsymbol{u}_i) \cdot \nabla_i W_{ij} V_j + \mathcal{D}_i^\rho, \\[2mm] \rho_i \dfrac{d\boldsymbol{u}_i}{dt} = \boldsymbol{F}_i^p + \boldsymbol{F}_i^v + \boldsymbol{F}_i^{st} + \rho_i \boldsymbol{g} + \sum_j (\rho_j \boldsymbol{u}_j \otimes \delta\boldsymbol{u}_j + \rho_i \boldsymbol{u}_i \otimes \delta\boldsymbol{u}_i) \cdot \nabla_i W_{ij} V_j, \\[2mm] \dfrac{dm_i}{dt} = \left[\sum_j (\rho_j \delta\boldsymbol{u}_j + \rho_i \delta\boldsymbol{u}_i) \cdot \nabla_i W_{ij} V_i V_j + \mathcal{D}_i^m \right] \eta, \\[2mm] \dfrac{d\boldsymbol{r}_i}{dt} = \boldsymbol{u}_i + \delta\boldsymbol{u}_i, \quad V_i = m_i/\rho_i, \quad p = c_0^2(\rho - \rho_0), \end{cases} \tag{3}$$

where $\boldsymbol{F}_i^p$, $\boldsymbol{F}_i^v$ and $\boldsymbol{F}_i^{st}$ are the pressure, viscous and surface tension forces acting on the particle i.

The parameter η can be set equal to 1 or 0; in the latter case, the particle masses remain constant during the time evolution. Both the η values are investigated in [34] where it is clearly shown that the two different schemes are equivalent in terms of outputs. However, in the present work, we show that the error in the volume conservation, ϵ_V, exhibits different behaviours when η is 0 or 1. Therefore, the switch between the two schemes can be used to control volume errors.

For the sake of brevity, in the present work the notation $\boldsymbol{r}_{ji}$ indicates the differences of the particle positions $(\boldsymbol{r}_j - \boldsymbol{r}_i)$ and the same holds for the velocity fields $\boldsymbol{u}_{ji}$ and $\delta\boldsymbol{u}_{ji}$, while, for the generic scalar field the notation f_{ij} just indicates the dependency of the field f on the indices i and j.

The spatial gradients are approximated through convolution summations with a kernel function W_{ij}. This function has a compact support whose reference length is denoted by h which is referred to as "smoothing length". As in [34] a C2-Wendland kernel [35] is adopted in the present work and it depends on the particle distance $r_{ji} = \|\boldsymbol{r}_{ji}\|$, hence, the spatial derivatives of the kernel function are represented as follows:

$$\nabla_i W_{ij} = \boldsymbol{r}_{ji} \left(\frac{1}{r_{ji}} \frac{dW}{dr_{ji}} \right) = \boldsymbol{r}_{ji} F_{ij},$$

where the scalar function F_{ij} only depends on the particle distance r_{ji} and it is strictly positive (see also e.g. [36]).

The radius of the support of this kernel is $2h$. For two-dimensional simulations, the number of particles inside the support is chosen in order to satisfy the relation $2h = 4\Delta r$ while for three-dimensional simulations, $2h = 3\Delta r$ is adopted, where Δr is the initial particle spacing.

The vector $\delta\boldsymbol{u}$ is the Particle Shifting velocity adopted to regularize the particles' spatial distribution during their motion. The specific law adopted in the present work is given in Section Section 2.3. Accordingly, the time derivative d/dt used in (3) indicates a quasi-Lagrangian derivative [29], i.e.:

$$\frac{d(\bullet)}{dt} := \frac{\partial(\bullet)}{\partial t} + \nabla(\bullet) \cdot (\boldsymbol{u} + \delta\boldsymbol{u}),$$

since the particles are moving with the modified velocity $(\boldsymbol{u} + \delta\boldsymbol{u})$ and the above equations are written in an Arbitrary-Lagrangian–Eulerian framework. For this reason, the continuity and the momentum equations contain terms with spatial derivatives of $\delta\boldsymbol{u}$ (for details, see [34]).

Regarding the pressure and viscous forces $\boldsymbol{F}^p$, $\boldsymbol{F}_i^v$, they are expressed as:

$$\begin{cases} \boldsymbol{F}_i^p := -\sum_j \left(p_j + p_i\right) \nabla_i W_{ij} V_j, \\[2mm] \boldsymbol{F}_i^v := K \sum_j (\mu + \mu_{ij}^T) \pi_{ij} \ \nabla_i W_{ij} V_j, \qquad K := 2(n+2), \\[2mm] \pi_{ij} := \dfrac{\boldsymbol{u}_{ij} \cdot \boldsymbol{r}_{ij}}{\|\boldsymbol{r}_{ji}\|^2}, \qquad \mu_{ij}^T := 2 \dfrac{\mu_i^T \mu_j^T}{\mu_i^T + \mu_j^T}, \quad \mu_i^T := \rho_0 \left(C_S l\right)^2 \|\mathbb{D}_i\|, \end{cases} \tag{4}$$

where n is the number of spatial dimensions and C_S is the so-called Smagorinsky constant, set equal to 0.18 (see *e.g.* [37]). The viscous term in (4) contains both the effect of the physical viscosity μ and the one related to the turbulent stresses μ_i^T. The length $l = 4\Delta r$ is the radius of the support of the kernel W and represents the length scale of the filter adopted for the LES sub-grid model. $\|\mathbb{D}\|$ is a rescaled Frobenius norm, namely $\|\mathbb{D}\| = \sqrt{2\mathbb{D} : \mathbb{D}}$ (see [38]). In order to damp the turbulent eddy viscosity μ_T near the wall boundaries, a classical van Driest damping function is employed (see [39,40])

$$y_i^+ = y_i \frac{u_{\tau i}}{\nu}, \quad u_{\tau i} = \sqrt{\frac{\tau_{wi}}{\rho_i}}, \quad \tau_{wi} = \mu \left.\frac{\partial \boldsymbol{u}_i}{\partial \boldsymbol{n}_k}\right|_{wall},$$

where the normal gradient to the wall is evaluated considering the velocity $\boldsymbol{u}_i$ and the distance y_i of the ith particle from the wall and using $\boldsymbol{n}_k$ as the unitary vector to the wall associated to the kth node closest to the ith particle.

The terms $\mathcal{D}^m$, $\mathcal{D}^p$ are the numerical diffusive terms introduced by [24,34]:

$$\begin{cases} \mathcal{D}_i^m := 2\delta c_0 h \sum_j (m_j - m_i) F_{ij} \sqrt{V_i V_j}, \\[2mm] \mathcal{D}_i^\rho := 2 \sum_j \delta_{ij} \left[(\rho_j - \rho_i) - \dfrac{1}{2} \left(\langle\nabla\rho\rangle_i^L + \langle\nabla\rho\rangle_j^L\right) \cdot \boldsymbol{r}_{ji}\right] F_{ij} V_j, \\[2mm] \delta_{ij} := 2 \dfrac{\nu_i^\delta \nu_j^\delta}{\nu_i^\delta + \nu_j^\delta}, \qquad \nu_i^\delta := (C_\delta l)^2 \|\mathbb{D}_i\|, \end{cases} \tag{5}$$

where δ and C_δ are dimensionless constants set equal to 0.1 and 6 respectively (see for details [38,41]). The superscript L in (5) indicates that the gradient is evaluated through the renormalized gradient (for details see *e.g* [42]). When considering violent free-surface flow, $\|\mathbb{D}_i\|$ can reveal a singular behaviour in the limit $l \to 0$, especially during impacts, and it can reach unlimited values; therefore, in order to avoid stability issues, the terms μ_{ij}^T and δ_{ij} are limited with upper bounds equal to, respectively, $\mu_{ij}^T = 0.1 \, l \, c_0 \, \rho_0 / K$ and $\delta_{ij} = 0.1 \, l \, c_0$.

It is important to note that the corrections of the above term proposed in [43] to remove the "tensile instability" are not used in the present work since this instability can be prevented by particle shifting.

The surface tension force is represented as:

$$\boldsymbol{F}_i^{st} = -\sigma \, \kappa_i \, \boldsymbol{n}_i \, \delta_{\Sigma,i},$$

where σ is the surface tension coefficient, κ_i the local curvature of the interfaces close to the ith particle, $\boldsymbol{n}_i$ the unit vector normal to the interface and $\delta_{\Sigma,i}$ the interfacial function. To evaluate the three quantities, κ_i, $\boldsymbol{n}_i$ and δ_{Σ_i} the algorithm proposed in [44] was implemented. It is worth noting that the model implemented was also able to correctly predict the contact angle between the liquid and the tank wall. However, as also shown in [45], the correct prediction of the contact angle is not crucial for the dynamics of the present test-cases.

Finally, since the variations of the density field are supposed to be small, a linear state equation in (3) was adopted and the reference density value ρ_0 refers to the density along the free surface. The weakly-compressible regime (density variations smaller than 1%) arises when the speed of sound c_0 fulfils the condition:

$$c_0 \geq \max\left(10 U_{max}, 10\sqrt{(\Delta p)_{max}/\rho}\right), \tag{6}$$

where U_{max} and $(\Delta p)_{max}$ are respectively the maximum fluid speed and the maximum pressure variation (with respect to the pressure on the free surface) expected in the fluid domain (see *e.g.* [46,47]). To avoid small-time steps in numerical simulations, an artificial sound speed is generally chosen in SPH instead of the real physical value of c_0. Such a numerical sound speed has to satisfy, in any case, the constraint in Eq. (6) during the simulations.

2.3. Particle Shifting Technique (PST)

To regularize particle distribution during the SPH simulation, the Particle Shifting Technique (PST hereinafter) [29] is utilized with the shifting velocity $\delta\boldsymbol{u}$ in Eq. (3) written as:

$$
\begin{cases}
\delta\boldsymbol{u}_i^* = -\xi\,h\,U_{\max}\sum_j\left[1+R\left(\dfrac{W_{ij}}{W(\Delta r)}\right)^n\right]\nabla_i W_{ij}\,V_j\,, \\[3mm]
\delta\boldsymbol{u}_i = \min\left(\|\delta\boldsymbol{u}_i^*\|,\dfrac{\max_j\|\boldsymbol{u}_{ij}\|}{2},\dfrac{U_{\max}}{2}\right)\dfrac{\delta\boldsymbol{u}_i^*}{\left\|\delta\boldsymbol{u}_i^*\right\|}\,,
\end{cases}
\tag{7}
$$

where constants n and R are set to 4 and 0.2, respectively [48], and ξ is equal to 1 or 0 based if the PST is switched on or off (see Section 2.7).

The second equation in (7) limits the magnitude of the shifting velocity. The magnitude is proportional to the smoothing length h and therefore it reduces as the spatial resolution increases, which ensures the particle moving in a quasi-Lagrangian fashion. Satisfying the kinematic boundary condition on the free surface implies that the normal component of $\delta\boldsymbol{u}$ must be nullified, hence, the Eq. (7) needs to be modified when the i-the particle is close to the free surface (see [29,49], and [28]).

Although the use of the Particle Shifting Technique helps to increase the accuracy of the scheme, it also causes the loss of the exact conservation of the angular momenta [34]. In addition, the PST has a large effect on the volume accumulation errors. Different Particle Shifting law leads to different magnitude of the volume error, which was originally discovered in [29] and also recently studied in [30,32].

2.4. Time integration

The system (3) is integrated in time by using a 4th-order Runge–Kutta scheme. The vector $\delta\boldsymbol{u}$ vector and the diffusive terms are kept constant during the Runge–Kutta sub-steps, which means that a frozen-diffusion algorithm is used (see [42]).

The time step Δt is obtained with the following equations:

$$
\begin{cases}
\Delta t_v = 0.125\left(\dfrac{h^2}{\nu}\right),\quad \Delta t_a = 0.25\,\min_i\sqrt{\dfrac{h}{\|\boldsymbol{a}_i\|}},\quad \Delta t_c = K_c\left(\dfrac{h}{c_0}\right), \\[4mm]
\Delta t_{st} = 0.25\sqrt{\dfrac{\rho\,h^3}{2\,\pi\,\sigma}},\qquad \Delta t = \min(\Delta t_v,\Delta t_a,\Delta t_c,\Delta t_{st}),
\end{cases}
\tag{8}
$$

where $\|\boldsymbol{a}_i\|$ is the particle acceleration and Δt_a is a constraint on the particles' advection, i.e. for accuracy reasons particles should not move with a displacement higher than their size Δr (for more details see [50]).

The parameter K_c is the Courant–Friedrichs–Lewy number, whose value depends on the adopted time integration scheme, on the chosen kernel function and on the specific SPH schemes adopted (see Section 2.7).

Generally, Δt_c represents the most restrictive condition, however, the violent sloshing flows studied in this work involve strong water impacts, hence, during such stages, the most restrictive constraint can be the advective one i.e. Δt_a. In this work, the Reynolds and the Weber numbers treated are sufficiently high so that the constraints on the viscous diffusion process Δt_v and on the surface tension Δt_{st} are less restrictive.

2.5. Solid wall boundary with a robust bouncing-back scheme

The sloshing flows studied in this research are confined in rectangular (2D) or cuboids (3D) tanks, therefore, the simple ghost-particle model by [20] was adopted to enforce the solid boundary condition. However, due to the violent flows studied, a robust bouncing-back technique is also needed to prevent the penetration of the fluid particles into the solid region. More in detail, when a fluid particle is approaching a solid wall and its distance from the wall is less than $\Delta r/4$, its normal velocity component is changed in sign, leaving unchanged the tangential one. Regarding the distance d_i of the generic particle i from the solid wall, this is evaluated with:

$$
d_i = |(\boldsymbol{r}_i - \boldsymbol{r}_k)\cdot \boldsymbol{n}_k|,
$$

where $\boldsymbol{r}_k$ is the position of the nearest solid wall node to the ith particle, and $\boldsymbol{n}_k$ is the normal unit vector associated with the kth node. The solid walls are discretized with the same spatial resolution adopted for the fluid domain.

It is worth noting that the bouncing-back technique acts on few particles, therefore its effect on the particles' momenta is always negligible.
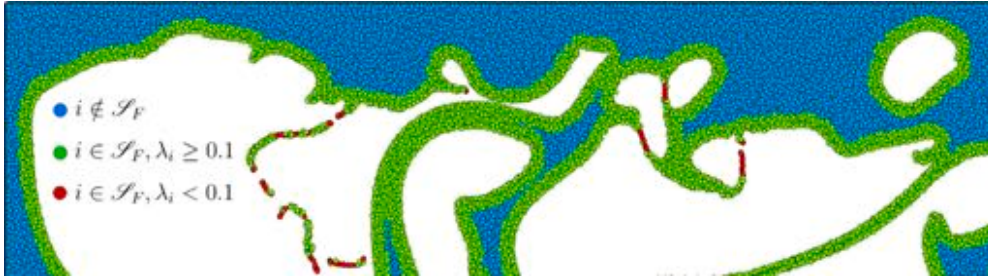
Fig. 1. Particles in thin jets and drops (red), free-surface region (green) and internal fluid (blue). (For interpretation of the references to colour in this figure legend, the reader is referred to the web version of this article.)

Table 1
Summary of the SPH models adopted for the simulations in this work.

SPH model	δ	C_δ	ξ	η	K_c
Standard SPH	0	0	0	0	1.0
δ-SPH	0.1	6	0	0	1.2
δ^+-SPH	0.1	6	1	0	1.3
δ-ALE-SPH	0.1	6	1	1	1.3
δ^+-ALE-SPH	0.1	6	1	Dynamical Switch 1/0	1.3

2.6. Enforcement of dynamic boundary conditions on thin jets and drops: the EdBC correction

Besides the η switch discussed at the beginning of this section, a second key factor that may help in reducing the error on the volume is the following correction:

$$p_i = 0 ; \qquad \rho_i = \rho_0 ; \qquad V_i = \frac{m_i}{\rho_0} , \qquad \forall i \in \mathscr{S}_F \quad \text{with } \lambda_i < 0.1 , \qquad (9)$$

where $\mathscr{S}_F$ denotes the region of the fluid domain close to the free surface, that is the free-surface particles and their neighbouring particles (see Fig. 1).

The free-surface particles are detected through the algorithm described in [51]. The quantity λ_i is the minimum eigenvalue of the matrix:

$$\mathbb{L}_i := \sum_j \left(\boldsymbol{r}_{ji} \otimes \boldsymbol{r}_{ji} \right) F_{ij} V_j . \qquad (10)$$

The variation of particle displacements is very limited during the Runge–Kutta sub-steps, so the evaluation of Eq. (10) is updated just at the end of each time step.

For the interior particles, which are regularly distributed and which have a large enough number of neighbouring particles, λ_i is very close to 1. Conversely, λ_i reduces its value for the particles belonging to $\mathscr{S}_F$ set. In Fig. 1 it is evident that the particles with $\lambda_i < 0.1$ are a limited number corresponding to the particles belonging to drops and on thin jets. It follows that the number of particles where the correction EdBC (9) acts are very small, however, this correction may have a large effect on the volume errors ϵ_V, indeed, most of these errors come from the fragmentation of the free-surface. In the present work, $\lambda_i < 0.1$ is used for all the test cases, however, we note that the value of the threshold could be changed for different $h/\Delta r$ ratios and different kernel functions.

2.7. Summary of the adopted SPH schemes

Considering the SPH scheme described in Section 2.2 we can downgrade it by switching off some of the parameters. For example, putting $\eta = \delta = C_\delta = \xi = 0$ the Standard SPH scheme is recovered. Among the possible combinations of the above parameters we selected five different SPH models reported in Table 1 with the choice of different parameters, where K_c is the Courant–Friedrichs–Lewy number defined in Section 2.4.

In Section 5 it is discussed how the EdBC correction is effective on the different SPH models in both 2D and 3D frameworks.

3. Evaluation of geometric volume for free-surface flows

For all the cases treated in the present work (see more in Section 4), the liquid is initially contained in a rectangular tank which occupies a volume $V_0 = LHW$, where L is the tank length, H the filling height and W the tank thickness (set equal to $W = 1$ for the 2D cases). In this section, the methods to evaluate in run-time the geometric volume $\mathcal{V}$ of the particle system are introduced. As a consequence, the relative volume error ϵ_V with respect to the initial value V_0 can be obtained (see Eq. (2)). During the simulation, the time histories of $\epsilon_V(t)$ is stored in order to analyse it for the five different SPH models selected. In this section two methods of evaluating $\mathcal{V}$ are introduced while the other two techniques are described in Appendix.
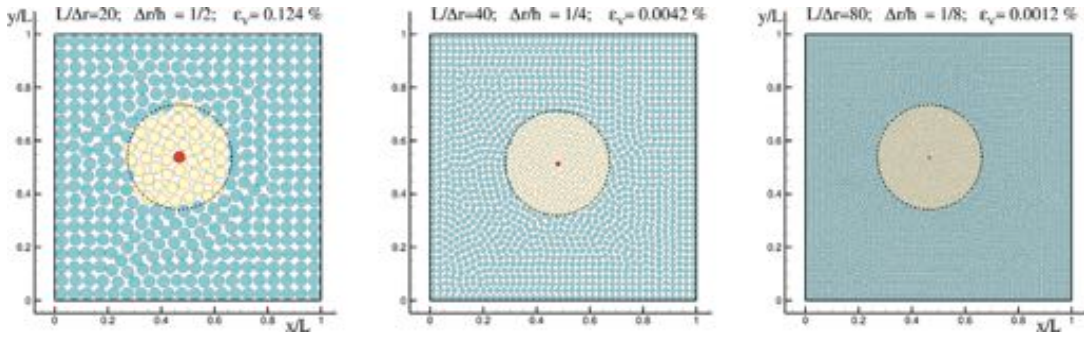
Fig. 2. Relative error ϵ_V on the evaluation of the volume of a square domain $L \times L$, varying the ratio $\Delta r/h$, i.e. the number of particles present in the kernel support. The particles are displaced in the domain using the packing algorithm described in [53].

3.1. Method #1: Evaluation of geometric volume using the SPH kernel function

Following [52] the geometrical volume of the ith particle can be directly evaluated through the kernel summation, i.e.:

$$\mathcal{V}_i = 1/\sum_j W_{ij}. \tag{11}$$

This formula can be derived from the original SPH model Eq. (1) assuming the particle masses present a low gradient inside the kernel support so that $m_j \simeq m_i$.

Using formula (11), the error ϵ_V depends on:

(i) the regularity of the particles' spatial displacement and
(ii) the number of neighbouring particles, i.e. the ratio $\Delta r/h$.

An example of this evaluator is given in Fig. 2 for the calculation of the area of a squared domain. The particles are distributed on the squared domain using the packing algorithm presented in [53] in order to have the distribution of the particles similar to that predicted by an SPH simulation. In this example, bi-periodic boundary conditions are used to avoid the truncation of the kernel support. The results reported in Fig. 2 show that a ratio $h/\Delta r = 2$ is enough for getting a good evaluation of $\mathcal{V}$, indeed, an error of order 0.1% is small enough with respect to the one evaluated in our simulations characterized by a magnitude of one or even two orders of magnitude greater than.

As remarked above, the formula (11) for $\mathcal{V}_i$ cannot be used within the SPH schemes when a free-surface is present because of the kernel support truncation of the particles that are in the neighbourhood of the liquid interface. The particle densities are evaluated through the SPH Eq. (3) and the SPH volumes follow the equation $V_i = m_i/\rho_i$, as already remarked, and they are not more directly correlated with the positions of the particles and they cannot be used to evaluate ϵ_V.

Therefore, the formula (11) needs to be corrected when a free-surface is present. For all the particles belonging to $\mathscr{S}_F$ the formula (11) cannot be used since the kernel support is uncompleted. However, considering that close to the free-surface the pressure goes to zero, in first approximation we can consider that the particles in $\mathscr{S}_F$ have pressure close to zero, hence, a density close to ρ_0 which corresponds to a particle volume close to the initial one $V_{i0} = \Delta r^2$. Therefore, the first method to evaluate the error volume can be:

$$\epsilon_V^{(1)} = \frac{\sum_i \mathcal{V}_i}{V_0} - 1, \qquad \mathcal{V}_i = \begin{cases} \dfrac{1}{\sum_j W_{ij}} & \forall i \notin \mathscr{S}_F, \\ V_0 = \Delta r^2 & \forall i \in \mathscr{S}_F. \end{cases} \tag{12}$$

For the approximation made, the above equation cannot be used run-time in the SPH scheme (3) instead of the continuity equation, however, as shown in Section 5, it can be used for the time evaluation of the volume error ϵ_V.

Regarding the Standard SPH, the accumulation of the volume error is expected to be very limited. Indeed, the continuity equation of the Standard SPH is given through the time derivation of Eq. (11):

$$\frac{d\mathcal{V}_i}{dt} = \mathcal{V}_i^2 \sum_j \boldsymbol{u}_{ji} \cdot \nabla_i W_{ij}, \tag{13}$$

substituting the latter in the continuity equation we obtained:

$$\frac{d\rho_i}{dt} = \frac{d\left(\frac{m_i}{\mathcal{V}_i}\right)}{dt} = -m_i \sum_j \boldsymbol{u}_{ji} \cdot \nabla_i W_{ij} \simeq -\rho_i \sum_j \boldsymbol{u}_{ji} \cdot \nabla_i W_{ij} V_j. \tag{14}$$

Therefore, the error $\epsilon_V^{(1)}$ is just linked to the error made by the time integration of this equation with the assumption $V_i \simeq V_j$.
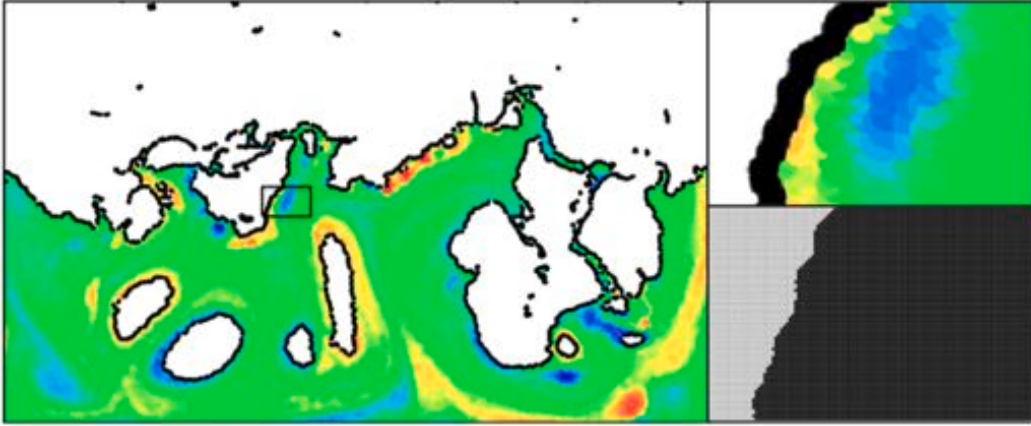
Fig. 3. Sketches of how works the graphical method. On the left panel: the frame of the numerical simulation. On the right panel: the zoom of the squared area. In particular, the bottom figure shows the snapshot after the conversion in binary pixels: black with a value equal to 1 for fluid regions and white with a value equal to 0 for the empty ones.

3.2. Method #2: Evaluation of geometric volume using the graphical method

This second method is used as a validation of the previous one. It is based on the analysis of the positions of the particles during the time evolution through an examination of saved snapshots, exploiting graphical code built on MATLAB©. The particles are represented as coloured circles and their size has to be tuned in order to have a complete overlapping between the particles avoiding empty spaces. Each snapshot is then elaborated, converting the pixel of fluid in black and associating a value equal to 1 while the void regions are set in white associating the value of 0 (see Fig. 3). The second approximation for the error ϵ_V is given as:

$$\epsilon_V^{(GM)} = \frac{N_{pixel}^{black}}{N_{pixel}^{tot}} - 1, \tag{15}$$

where N_{pixel}^{tot} are the total number of the pixels of the image processed while N_{pixel}^{black} are the number of pixels representing the fluid region which are coloured in black.

It is worth noting that the evaluation in time of $\epsilon_V^{(GM)}$ requires saving many configurations of particles during the whole simulation. However, for long-time periodic sloshing, this is not possible if we want to limit the total size of the output files. For this reason, in the longest periodic sloshing cases presented in this work, the particle configurations are stored only for the last part of the simulation.

The extension of this graphical method to the 3D framework is more difficult to apply and manage. In fact, at different time instants, the particle domain should be cut on several slices where the proposed algorithm needs to be applied.

4. Description of the sloshing problems considered for the validation of SPH models

In the present work, four different violent sloshing flows in partially filled rectangular tanks are investigated through experimental tests and numerical simulations with single-phase SPH models. These test-cases were designed within the European Project SLOWD "Sloshing Wing Dynamics". The project aimed to investigate the fuel sloshing damping effect to reduce the design loads on aircraft wings. In this project, an extensive experimental campaign was conducted to study slosh-induced damping in an excited tank filled with liquid.

The selected benchmarks differ not only in the tank's size but also in the sloshing dynamic and more in detail they are:

1. Shallow Water (SW) — periodic heave sloshing (SAP);
2. Intermediate Water (IW) — heave sloshing in decay motion (UPM);
3. Intermediate Water (IW) — periodic sway sloshing (INM1);
4. Intermediate Water (IW) — periodic sway sloshing with large amplitude motion (INM2).

The characteristic lengths of the tank geometry are L, D and W which are respectively the length, the height and the width of the tank. In the non-inertial frame of reference moving with the tank, the x-axis is set along the tank length L, y-axis along the height D and z-axis along the tank width W. The origin of the xy axis is set on the left-bottom corner of the tank. The filling height is indicated with H. The tank oscillating motion is characterized by an excitation amplitude A and by a period of oscillation T. For the second test-case (UPM) the amplitude exponentially decreases in time from its initial value A.

Table 2
Geometric tank size of test cases.

Test N°	Label	L (cm)	D (cm)	W (cm)	H (cm)	M_L (Kg)
#1	SAP	11.72	2.72	7.80	1.36	0.124
#2	UPM	10.0	6.00	6.00	3.00	0.180
#3	INM1	100	100	10.0	35.0	34.9
#4	INM2	100	100	10.0	35.0	34.9

Table 3
Parameters of the sloshing test cases.

	A (cm)	$f = 1/T$ (Hz)	ΔE (mJ)	$\Delta W = \Delta E/T$ (mW)
SAP	0.43	13.0	7.67	99.7
UPM	5.70	6.51	489	3185
INM1	5.00	0.909	1426	1298
INM2	10.0	1.00	6889	6889

Table 4
Dimensionless sloshing parameters.

	Sloshing dynamic	H/L	A/L	$\omega(H/g)^{1/2}$	Re	We
SAP	Heave — Periodic SW	0.12	0.037	3.04	4970	25.0
UPM	Heave — Decay motion IW	0.30	0.57 to 0	2.26	70,100	2240
INM1	Sway — Periodic IW	0.35	0.05	1.08	649,000	16,530
INM2	Sway — Periodic IW	0.35	0.10	1.19	649,000	16,530
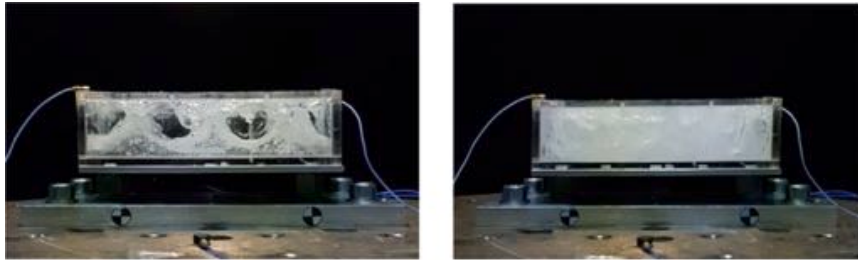
Fig. 4. Experimental snapshots of two different SAP test-case sloshing flows with the frequency of the vertical oscillation equal to $f = 13$ Hz and two acceleration amplitudes respectively equal to $a_0 = 1.5g$ and $a_0 = 3g$ [54].

The fluid mass is indicated with $M_L = \rho\, L\, H\, W$, the reference kinetic energy with $\Delta E = 1/2\, M_L\, (A\omega)^2$, where $\omega = 2\pi/T$. The related reference mechanical power is determined with $\Delta W = \Delta E/T$.

Considering $U_{ref} = \sqrt{gH}$ as a reference velocity of the studied sloshing flows, the Reynolds number is defined as Re $= \sqrt{gH}\, H/\nu$. The Weber number is defined as We $= \rho_0\, U_{ref}^2\, H/\sigma$. In most of the sloshing flows water is used as liquid, therefore the density, kinematic viscosity and surface tension are: $\rho = 1000$ kg/m^3, $\nu = 10^{-6}$ m^2/s and $\sigma = 0.0727$ N/m. For the second test-case (UPM) Re and We numbers need to be multiplied by 4.3 and 18.5 respectively, indeed, because of the large amplitude motion of the tank, the reference velocity is $4.3\sqrt{gH}$. For easier reading, the values of all quantities involved for all 4 test-cases are summarized in Tables 2–4, together with dimensionless quantities.

4.1. Test-case #1 (SAP)

Test-case #1 belongs to a large experimental campaign characterized by a tank subjected to a harmonic vertical acceleration with the following law:

$$y_{tank}(t) = -A\cos(\omega\, t),$$

where several frequency and vertical acceleration values are investigated experimentally in [54] and numerically in [55].

In the experiment, the motion of the tank was imposed by a controlled electrodynamic shaker able to force a vertical sinusoidal displacement as shown in the snapshots of Fig. 4 for two tested conditions. In particular, in the present work, we limit our analysis to the case with $A = 0.43$ cm and $f = 1/T = 13$ Hz which correspond to a maximum acceleration equal to $a_0 = \omega^2\, A \simeq 3g$.

From a physical point of view, the high vertical accelerations make the free surface unstable, reaching a nonlinear chaotic regime of the liquid with violent impacts on the ceiling and on the bottom of the tank with a significant fragmentation of the free surface.
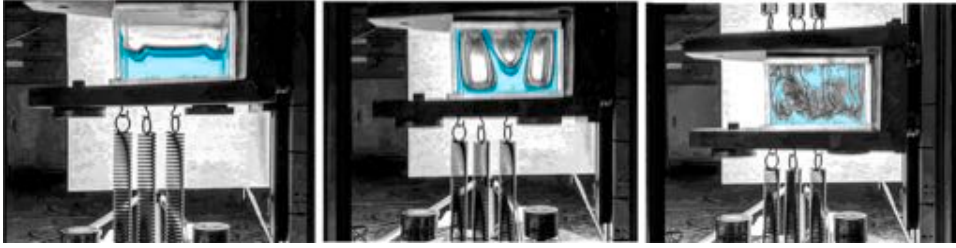
Fig. 5. Experimental snapshots at three different time instants, $t = 0.91T$, $t = 1.05T$ and $t = 8.47T$, of the vertical sloshing water tank carried out for UPM test-case [56].
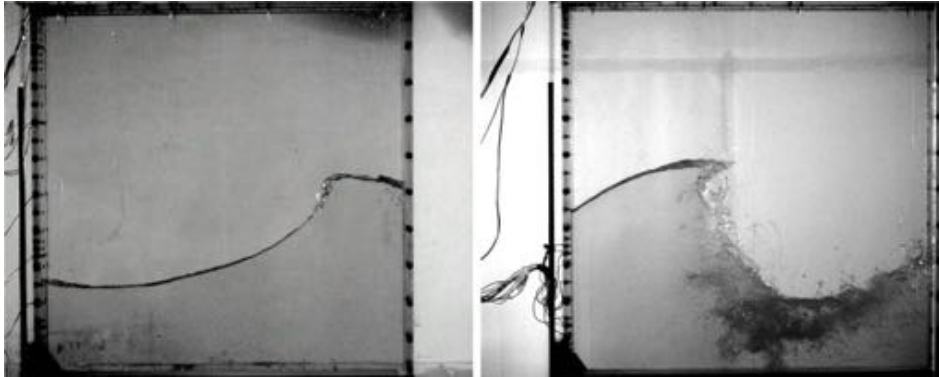

Fig. 6. Experiments snapshots sloshing sway respectively on the left-side INM1 ($A = 0.05L$, $T = 0.870\,T_1$ s) and right-side INM2 ($A = 0.10L$, $T = 0.793\,T_1$).

4.2. Test-case #2 (UPM)

For this test-case the tank is connected to a set of six springs arranged three on the upper and three on the lower side. The tank is filled up to 50% of its volume (*i.e.*, $H = 3$ cm) with water and when the springs are released, the tank starts oscillating at a characteristic frequency of about $f_0 = 6.51$ Hz as shown in Fig. 5. At the time $t = T$, the tank reaches its maximum vertical displacement $2A = 1.14L$ and a maximum acceleration $a_{max} \sim 8.8g$. The experimental campaign of this problem is described in detail in [56]. Because of the large amplitude motion and the high frequency of oscillation also for this test-case the flow is characterized by violent free-surface deformation with energetic fragmentation phenomena. The vertical motion of the tank decays in time under the action of the friction force and the sloshing dissipation; after 25 periods the tank is practically stopped, while due to the high Reynolds number (Re = 70,100), the liquid sloshing persists for a larger time range.

This case was also analysed numerically in [23,45,57,58] and performed with two different numerical approaches in [59]. For the sake of clearness, in the previous works, the Reynolds number is not referred to filling height H but to the tank length L, hence, it is equal to $Re_L = 233,000$.

4.3. Test-case #3 and #4 (INM1 and INM2)

In Test-case #3 and #4 periodic sloshing flows in the horizontal direction are considered. The excitement of the tank is performed with a pure-sway forced motion with sinusoidal horizontal law:

$$x_{tank}(t) = A \sin(\omega t),$$

with an oscillation period $T = 2\pi/\omega$ that is close to the first linear sloshing natural period $T_1 = 1.265$ s. It follows that large motions of the free-surface are induced by breaking wave events and the occurrence of intense water impacts on the tank's lateral side. The filling depth for both cases is $H = 0.35L$ while two different values of amplitude $A = 5$ cm and $A = 10$ cm are used. Conversely, the periods of oscillation are quite similar to $T = 1.1$ s and $T = 1$ s (see Table 3). Fig. 6 shows two-time instants during the test INM1 (left) and INM2 (right). During the test INM1 gentle breaking wave events develop, conversely, because of the larger motion amplitude $A = 10$ cm, INM2 is characterized by a more violent sloshing flow with a significant fragmentation of the free surface.

5. Numerical results and discussions

All the test-cases were performed with No-Slip boundary conditions on the solid wall to capture the effect of the friction forces on the later wall. The spatial resolution adopted in the simulations is high enough to resolve the boundary layer region which always

Table 5
Parameters adopted in the SPH simulations of the four sloshing tests.

	c_0 (m/s)	$N = H/\Delta r$	$\overline{\Delta t}$ (μs)	$\overline{\Delta t}\, c_0/h$
SAP #1	10	200	13	0.95
UPM #2	40	800	2.4	1.28
INM1#3	20	200	241	1.38
INM2#4	20	200	241	1.38

Table 6
Duration t_{end}, iteration times N_{iter}, particle numbers N_{part} and CPU time in the numerical simulations of the four sloshing tests.

	t_{end} (s)	t_{end}/T	N_{iter}	N_{part}	CPU time
SAP #1	7	91	542,000	345,000	3 days 4 h
UPM #2	4	26	1,650,000	2,135,000	64 days
INM1#3	300	272	1,240,000	114,000	2 days 9 h
INM2#4	300	300	1,240,000	114,000	2 days 9 h

remains in a laminar regime. In any case, even using the Free-slip condition, the issue of volume conservation would be present for all the cases considered. As already stressed, for all the test-cases a single-phase SPH model was adopted. The good comparisons with the experimental data demonstrate that the effects related to any entrapment of air by the liquid are mainly negligible. Table 5 reports the artificial speed of sound adopted in the different test-cases, and the maximum spatial resolution $H/\Delta r$ adopted. The time step requested by the constraints of Eq. (8) in Section 2.4 is recorded in time and the average value is reported in both dimensional and dimensionless values in Table 5.

For the CPU costs, Table 6 reports the time interval simulated, the number of time steps, the number of particles adopted for the highest spatial resolutions and the CPU time requested. All the simulations ran on a Workstation equipped with CPUs Intel(R) Xeon(R) Gold 6128 CPU @ 3.40 GHz with 24 cores.

For the sake of brevity, for test-cases #1 the results of the five SPH models are presented while for test-cases #2, #3 and #4 we only report the δ^+-ALE-SPH results showing its ability to limit the volume errors together with the comparisons with available experimental data.

For such kind of violent sloshing flows the air effect can be relevant, however, the comparison of our results on the sloshing damping against the experimental data is quite good, therefore the role of the air seems to be not critical in this aspect. In [59] the single-phase SPH was compared with the two-phase Finite Volume Method, for the test-case #2. The air effect is quite evident in the flow details. However, the comparisons between the two codes on the slosh dissipation remain quite fair. For the SPH schemes, the volume conservation issue is more critical in single-phase with respect to two-phase models. In the latter, the presence of air particles with a pressure field linked to the occupied volume drastically limits the volume errors.

5.1. Test-case #1 (SAP) Shallow water — periodic heave sloshing

In this section, the first test-case is analysed. The tank motion is in the vertical direction and it is periodic see Section 4.1. Two Reynolds numbers are considered, i.e. Re = 494 and Re = 4940. The simulations at Re = 4940 correspond to the experiment test-cases and they were performed with and without the surface tension. In the presence of the free-surface the value of the Weber number is the same as in the experiments.

5.1.1. Test-case SAP at Re = 494 and without surface tension (We = ∞)

We started the test-case SAP by reducing the Reynolds number by a factor of 10 and ignoring the surface tension. This allows showing in a simpler way the main mechanism of the different tested five SPH schemes (see Table 1). Conversely, in the following subsection, the results of the numerical simulations with the Reynolds number tested in the experiment are presented and it will be shown that with higher Re the volume conservation issue can be even more demanding for the SPH schemes.

Fig. 7 shows the error $\epsilon_V^{(1)}$ for four different SPH models. For these results the EdBC correction has not been used, it is clear that the Standard SPH is the only model where the accumulation error on ϵ_V seems negligible.

All three models δ-SPH , δ^+-SPH and δ-ALE-SPH accumulate significant volume errors with negative sign i.e. the geometrical volume $\mathcal{V}$ is reducing. When using the PST (δ^+-SPH and δ-ALE-SPH models) the error on the volume conservation increases with respect to the result of δ-SPH. In the δ-ALE-SPH model (in which $\eta = 1$ and the particle masses change in time) $|\epsilon_V^{(1)}|$ increases so much as to make the simulation unstable, hence, it is impossible to perform the ninety oscillations of the tank with such an SPH model.

In Fig. 8 the EdBC correction is applied to all four SPH models. The use of the EdBC correction worsens the Standard SPH results. Concerning δ-SPH with the EdBC correction, the absolute level of error $|\epsilon_V^{(1)}|$ does not change but, on the contrary, the sign of the steepness of ϵ_V passes from negative to positive. The results in Fig. 8 show that $\epsilon_V^{(1)}$ is particularly reduced for δ^+-SPH when EdBC is adopted. Also in this model a change in the sign of the steepness is recorded. The δ-ALE-SPH model largely benefits when EdBC is used, even if, the volume error is still high and it remains the worst SPH model in this respect.
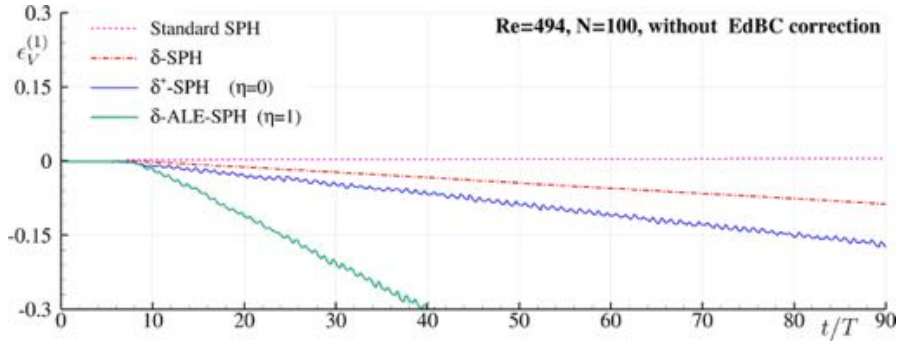
Fig. 7. Time histories of volume error of the sloshing problem simulated with different SPH models without EdBC correction.
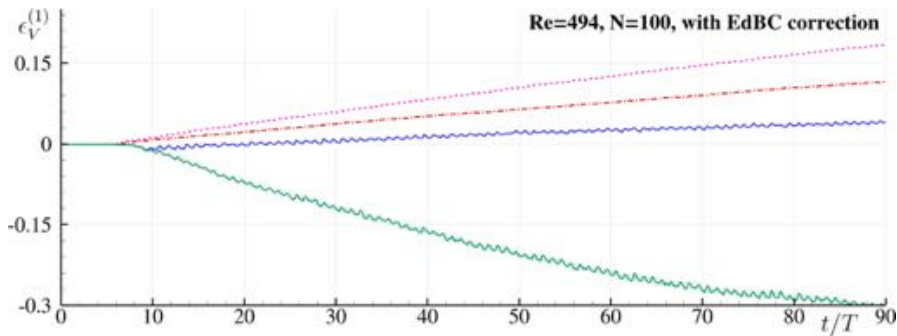

Fig. 8. Time histories of volume error of the sloshing problem simulated with different SPH models with EdBC correction.
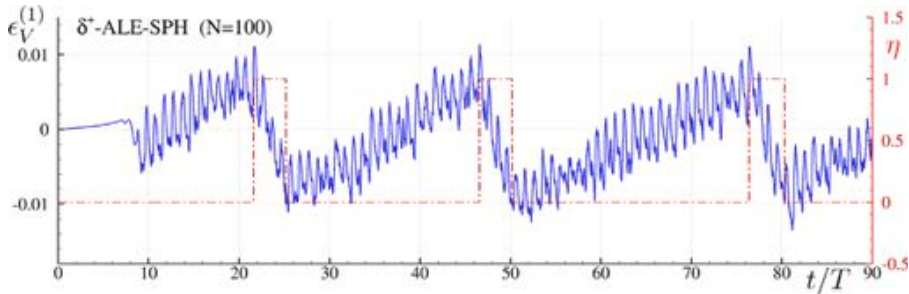

Fig. 9. Time histories of volume error (blue solid line) and η value (red dash line).

The change of the sign of the ϵ_V steepness is a key point for the present work since it gives the possibility to control the volume errors by switching from model to another.

In all the different test-cases simulated we always observe this change in terms of the ϵ_V slope when EdBC is used for the δ^+-SPH model. Thanks to these different temporal behaviours of ϵ_V, depending on the value of η, it is possible to control the volume error using a switch of the value of η during the simulation so that the δ^+-SPH and δ-ALE-SPH alternate over time. This combination of patterns is referred to in the following text as the δ^+-ALE-SPH model. The results are shown in Fig. 9 for the proposed δ^+-ALE-SPH scheme, where η changes over time when $|\epsilon_V^{(1)}|$ exceeds a given threshold. In this case, the threshold is set to an error of 1%.

It is worth noting that the oscillating time behaviour of $\epsilon_V^{(1)}$ does not allow the use of a threshold small as desired, even if, as shown later, increasing the spatial resolution, these oscillations reduced in amplitude allowing in general smaller threshold levels. Either way, for all simulations performed in this work the threshold of 1% is used assuming it is small enough.

It is worth pointing out that also the δ-SPH model can in principle be controlled switching the EdBC correction, however, for the sake of brevity, this investigation was not followed in the present work and is left for future studies.
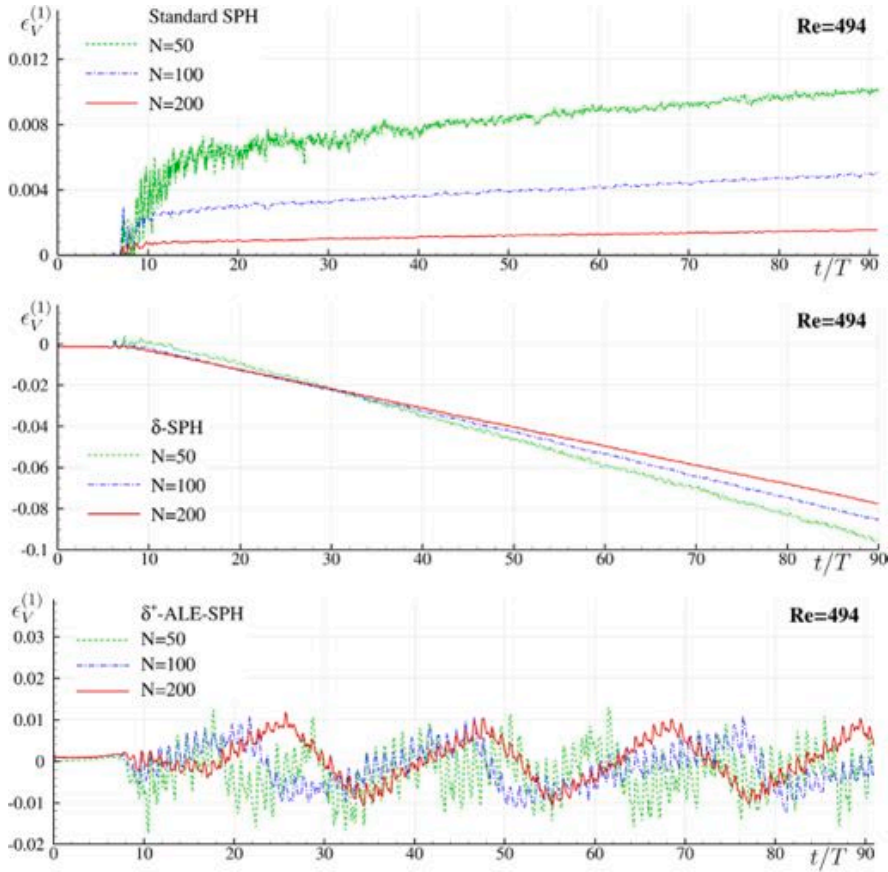
Fig. 10. Error on volume varying the spatial resolution. Top: Standard SPH. Middle: δ-SPH. Bottom: δ^+-ALE-SPH.

Fig. 10 depicts the time histories of $\epsilon_V^{(1)}$ changing the spatial resolution for the Standard SPH, δ-SPH and δ^+-ALE-SPH. With the Standard SPH, the error decreases with N and it always remains less than 1% during the simulation. As commented in Section 3, given the direct link with geometrical volume $\mathcal{V}$ and the continuity equation adopted in the Standard SPH, the above result is not surprising. Conversely, the diffusion added in the continuity equation for δ-SPH always leads to a relevant accumulation of the volume error, even at the highest spatial resolutions (this behaviour is also shared by δ-ALE-SPH and δ^+-SPH methods, which is not shown just for the sake of brevity).

In the case of the δ^+-ALE-SPH scheme the control mechanism, that employs the switch on the η parameter, confined the error within 1% for all the spatial resolutions. When N=200 the time histories show a smoothed behaviour in time and this means that in practice a further reduction of the threshold error below 1% would be possible.

Finally, to close this subsection a comparison between the two methods for evaluating the geometric volume, described in Section 3, $\epsilon_V^{(1)}$ (see Eq. (12)) and ϵ_V^{GM} (see Eq. (15)) is provided in Fig. 11. Discrepancies between the two algorithms are evident, however, their accuracy is enough good for the analysis performed in this work, indeed, they evolve in the same trend. The difference is due to the particle distribution of different SPH models as shown in Fig. 12. It is easy to observe that the Standard SPH is characterized by the most disordered configuration and therefore the difference between $\epsilon_V^{(1)}$ and ϵ_V^{GM} is the largest. On the contrary, this difference is quite limited for the δ^+-ALE-SPH scheme thanks to the PST which guarantees a uniform particle distribution.

Contour plots of the local error on volume, $\epsilon_{V\,i}^{(1)}$, for three different SPH models are depicted in Fig. 13 for the final time instant of the simulations. The fluid particles' distribution shows how the sloshing flow is quite energetic, inducing large deformation of the fluid domain as deeply discussed in [55]. From the middle plot of Fig. 13, it is quite evident that the volume contraction of the δ-SPH is the highest since the volume error $|\epsilon_{V\,i}|$ is greater than 10%. Conversely, for the Standard SPH most of the particles do not show sensible volume error, while in the δ^+-ALE-SPH the field of ϵ_V presents regions with low values of $\epsilon_{V\,i}^{(1)}$ and others with high values, a trend that ensures a volume average that remains bounded.

It is worth noting that, even if the Reynolds number in this first test-case is quite low, the damping due to the eddy viscosity is 26%, and this is linked to the high free-surface fragmentation. When using the real Reynolds number (see next subsections) the eddy viscosity contributes 56%, indeed, as shown, the turbulent regime starts to be quite energetic.
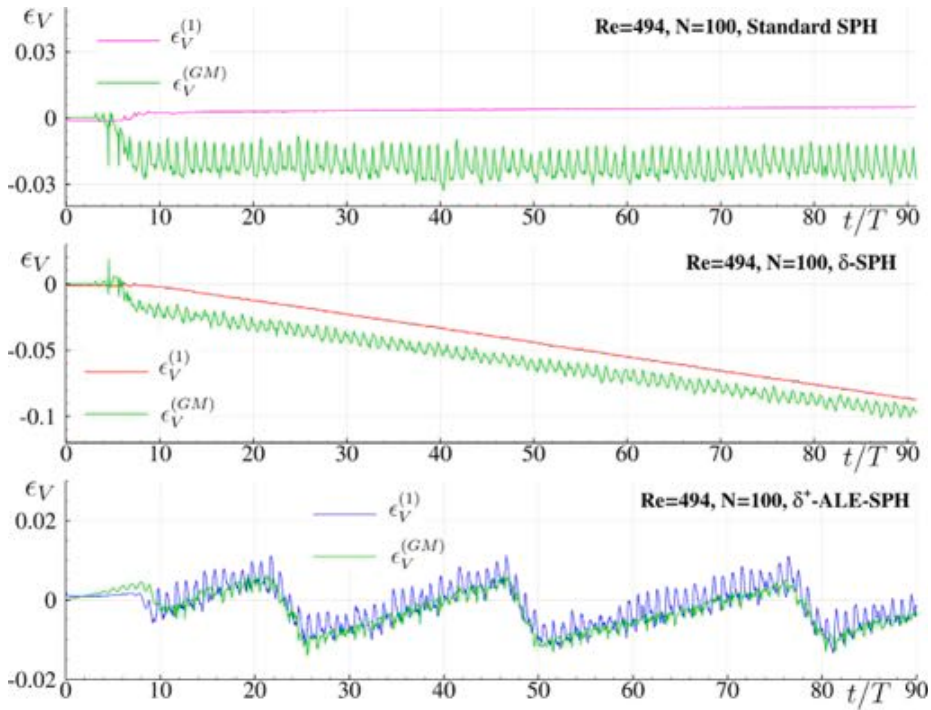
Fig. 11. Time histories of volume error. Comparison between the run-time procedure, $\epsilon_V^{(1)}$, and the graphical method ϵ_V^{GM} (see Section 3).
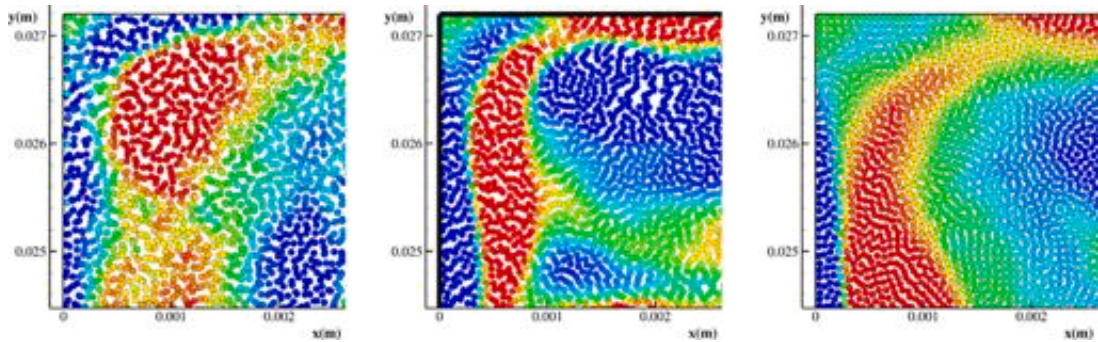

Fig. 12. The enlarged view around the left-top corner. Particles distribution for the SPH models during a roof liquid impact event: Standard SPH, δ-SPH and δ^+-ALE-SPH. Vorticity ranges between -5ω to $+5\omega$.

5.1.2. Test-case SAP at Re = 4940 and without surface tension

This subsection reports the test-case SAP with the real Reynolds number of the experiments. Being the Reynolds number higher ten times with respect to the previous subsection, the spatial resolution is doubled to $N = H/\Delta r = 200$.

Fig. 14 shows the time evolution of the volume error for the three SPH models: Standard SPH, δ-SPH and δ^+-ALE-SPH. The absolute error $|\epsilon_V^{(1)}|$ for the δ-SPH exceed the 10% while for Re = 494 it remains below this threshold. Again as in the previous subsection the Standard SPH presents a very low level of volume error. Regarding δ^+-ALE-SPH the switching of the η parameter (see Section 2.2) allows, also in this case, good control of the volume error.

Contour plots of the local error on volume, $\epsilon_V^{(1)}$, for three different SPH models are depicted in Fig. 15. As can be seen, with respect to the previous test-case the lower viscosity level leads to a more intense fragmentation of the free-surface which leads to a larger accumulation error on the fluid volume for the δ-SPH model. Conversely, for Standard SPH and δ^+-ALE-SPH schemes the $\epsilon_V^{(1)}$ fields present similarity with ones of the previous sub-section.

5.1.3. Test-case SAP at Re = 4940 and with real surface tension (We = 25)

Differently from the previous subsection, the test-case SAP is simulated with the real values of Reynolds number (Re = 4940) and surface tension (We = 25). Contour plots of the local error on volume, $\epsilon_{V\,i}^{(1)}$, for three different SPH models are depicted in Fig. 16. It
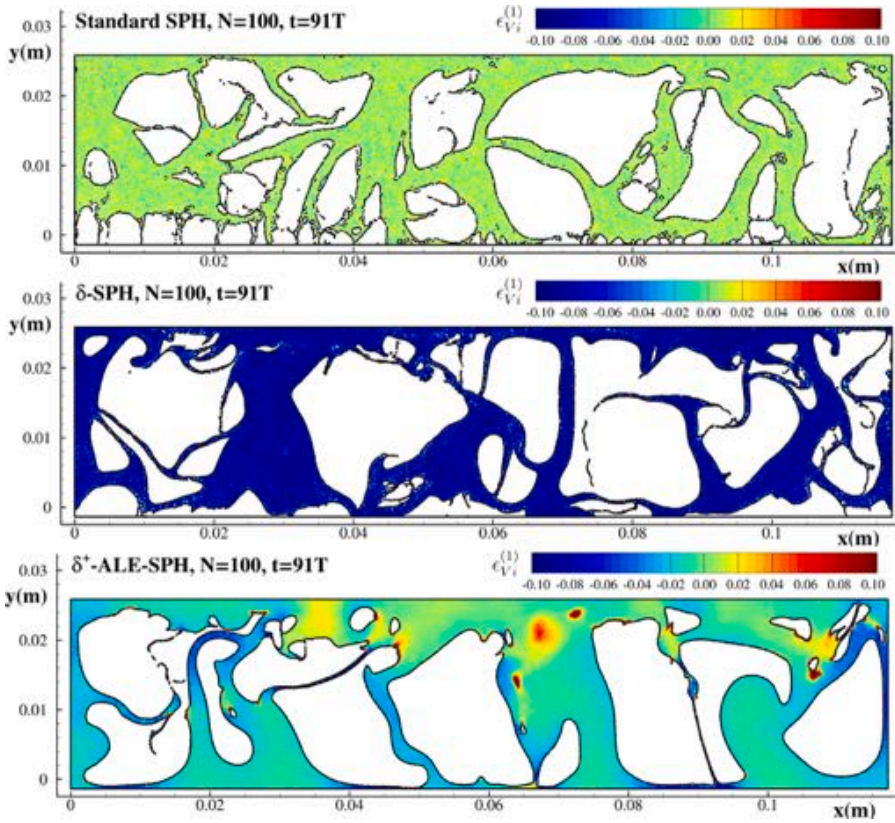
Fig. 13. Contour plot of the local error on volume, $\epsilon_{Vi}^{(1)}$, for three different SPH models: Standard SPH (top), δ-SPH (middle), δ^+-ALE-SPH (bottom) at Re = 494.
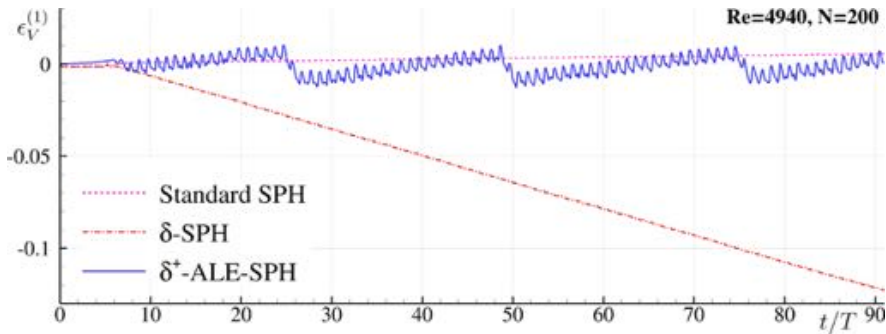
Fig. 14. Time histories of volume error. Comparison between the three SPH models.

is clear to note that, contrary to the previous test-case, the fragmentation of the present case is reduced by the action of the surface tension force. It follows that the accumulation error on the fluid volume is less as depicted in Fig. 17.

The top plot of this figure shows that the δ-SPH still accumulates in time the volume error but with a lower steepness. Regarding the δ^+-SPH the surface tension effects completely eliminate the appearance of secular term, hence, the volume errors always remain below 1% and there is not any necessity of changing η from 0 to 1.

The bottom plot of Fig. 17 shows the comparison of the volume error measured by $\epsilon_V^{(1)}$ and ϵ_V^{GM} during the simulation with δ^+-SPH model. The agreement between the two algorithms is quite good for the purposes of the present work.

Even if with the surface tension there is no need to change η, the use of the EdBC is still relevant as shown in Fig. 18. Especially for the lower particle resolution, where surface tension is still not able to prevent fragmentation, the accumulation of volume error is not negligible

As a summary of the test-case SAP results, Fig. 19 displays the rate of the slosh dissipated energy $\mathscr{P}$ made dimensionless with the reference power $\Delta W = \Delta E / T$ where $\Delta E = 1/2\, M_L\, (A\omega)^2$, see Table 3. The measure of the experimental value of $\mathscr{P}$ is reported
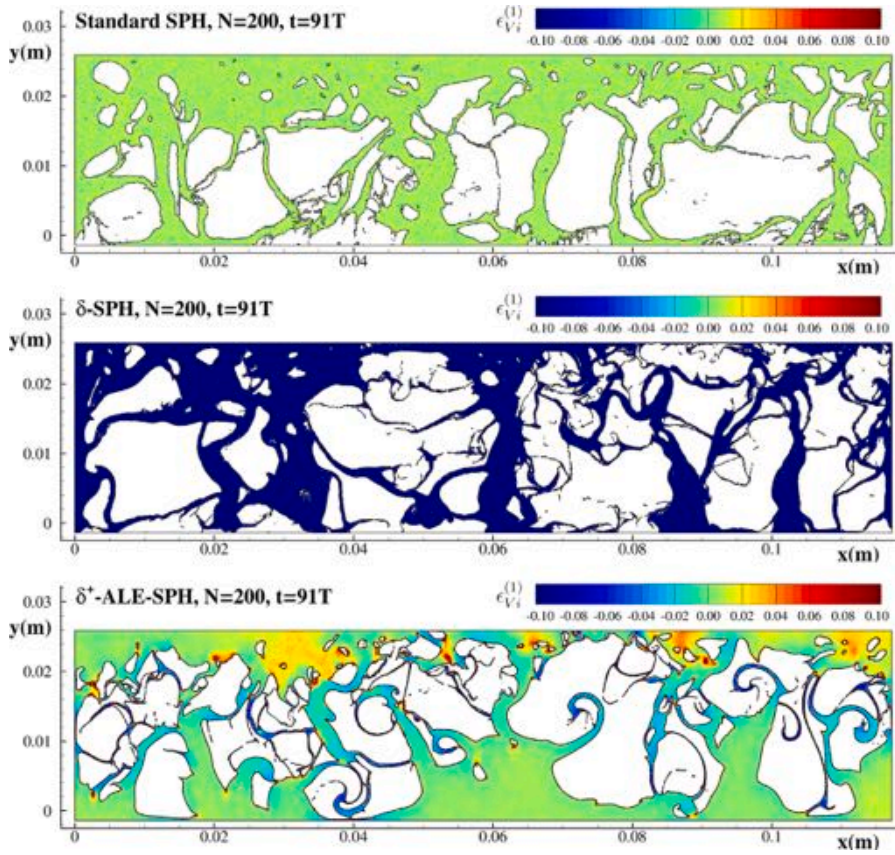
Fig. 15. Contour plot of the local error on volume for three different SPH models: Standard SPH (top), δ-SPH (middle), δ^+-ALE-SPH (bottom) at Re = 4940.

in [54]. Three SPH models are considered: Standard SPH, δ-SPH and δ^+-ALE-SPH models with four different spatial resolutions $N = H/\Delta r = 25, 50, 100, 200$. The three plots of Fig. 19 refer to the parameters investigated in the previous subsections, *i.e.* Re = 494 & We = ∞, Re = 4940 & We = ∞ and Re = 4940 & We = 25. One may find that, the δ^+-ALE-SPH model with the real physical parameter setting (Re = 4940 & We = 25) predicts the most accurate energy dissipation by comparing with the experimental value from [54]. Furthermore, the δ^+-ALE-SPH is the SPH model that exhibits the highest rate of convergence, indeed, the difference of $\mathcal{P}$ at N=100 and N=200 are quite small. As stressed in [55] the overestimation with respect to the experimental data of the δ^+-ALE-SPH model is linked to the 2D framework indeed 3D effects are not completely negligible for this test-case. It is worth noting that for the case Re = 4940 & We = ∞ none of the SPH models converge with the spatial resolution N, indicating that the scale of the turbulent eddies is still not well resolved. Regarding the δ-SPH , this model always gives the lowest results and this is mainly linked to the worst behaviour on the volume conservation. For the case with Re = 4940 & We = ∞ this SPH model shows even a divergence when increasing the spatial resolution.

5.2. Test-case #2 (UPM). Intermediate water — heave sloshing with decay motion

In this section, the heave sloshing with decay motion, described in Section 4.2, is analysed using three SPH models: the Standard SPH, δ-SPH and δ^+-ALE-SPH models. As for the test-case #1 results are compared against the experimental measure of the slosh dissipation [23,57–59]. Fig. 20 depicts the time histories of the vertical displacement of the tank. At time $t = T$ the tank reaches the maximum vertical elevation.

As remarked in the previous studies [23,57–59], being the Weber number (We = 2240) enough large, the surface tension effect on the slosh dissipation is negligible. However, its effect on the volume error can still be quite relevant. Therefore, also in this section, SPH simulations were performed both with and without the surface tension as in the previous test-case (SAP).

5.2.1. Test-case UPM at Re = 70,100 without surface tension (We = ∞)

Fig. 21 shows the fluid configurations for six-time instants. As commented in [58] the flow initially evolves with a Rayleigh–Taylor instability where the free surface deforms developing different liquid jets. Then, the fluid impacts the tank wall ceiling with the production of lateral jets. After this initial stage (first row of Fig. 21) the fluid starts a series of cyclical impacts against the
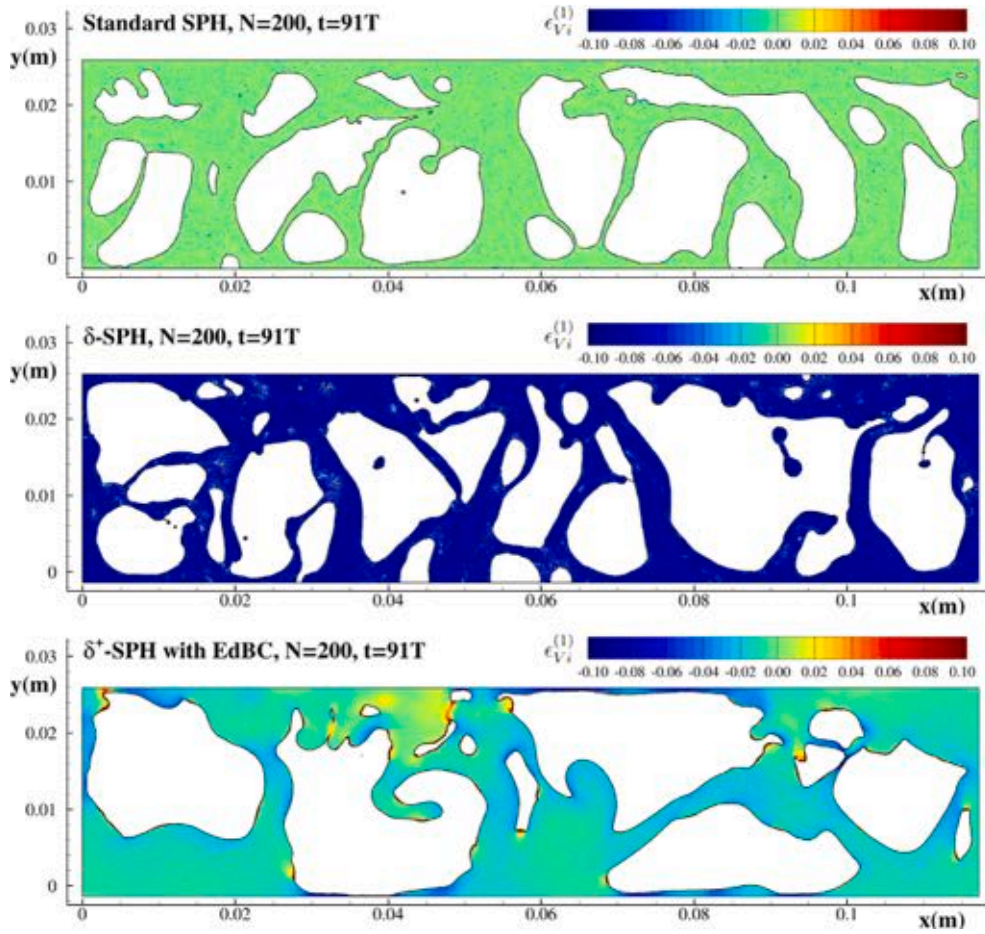
Fig. 16. Contour plot of the local error on volume $\epsilon_{V i}^{(1)}$ for three different SPH models: Standard SPH (top), δ-SPH (middle), δ^+-ALE-SPH (bottom) at Re = 4940 and We = 25.

bottom of the tank (second row of Fig. 21). The fluid is mostly fragmented in multiple jets and the energy is mainly dissipated in free-surface reconnections and the consequent generation of vorticity. At $t > 16T$ the impacts of the liquid on the roof become rarer and weaker and the flow enters a more conical lapping regime (*i.e.* the acceleration of the tank becomes less intense than the acceleration of gravity, see line bottom of Fig. 21).

In Fig. 21 the particles are coloured with the local volume error $\epsilon_{V i}$. As in the previous test-cases the δ^+-ALE-SPH model is able to maintain a limited averaged value of the volume error.

Fig. 22 depicts the time histories of volume errors $\epsilon_V^{(1)}$ and ϵ_V^{GM} evaluated with both the algorithms of Section 3. The geometrical volume increases by about 1% up to $t \simeq 7.7$, then, thanks to the η switch, the volume decreases to about -1% within a time range of one second and then goes up slowly to the zero error level after the second *eta* switch.

It is worth noting that, for $t > 18T$, the flow motion largely decays in intensity and consequently, the volume error stops drifting. In this problem, just two η switches are necessary to limit the volume error within the 1% level. This is also shown in Fig. 23 for three different spatial resolutions. In the same figure, it is clear that the increasing of the spatial resolution takes more time to reach the error limit of 1% delaying in time the switch of the η parameter. It should be underlined that within the previous articles [23,58,59] the simulations are performed without the correction proposed in this article. Since the UPM test case is limited in time to 26 oscillation periods with an amplitude that quickly reduced in time, the volume errors were limited below 10% and luckily those errors do not affect significantly the evaluation of the sloshing dissipation.

5.2.2. With surface tension (We = 2240)

As remarked in [23,58,59], since the Weber number is quite high, the surface tension plays a marginal role in the slosh dissipation, as further commented on at the end of this section. Plots in Figs. 24 and 25 display the time history of the volume error. Conversely to the test-case #1 (see Section 5.1) in this benchmark case the switch of η is still necessary even when the surface tension is present.
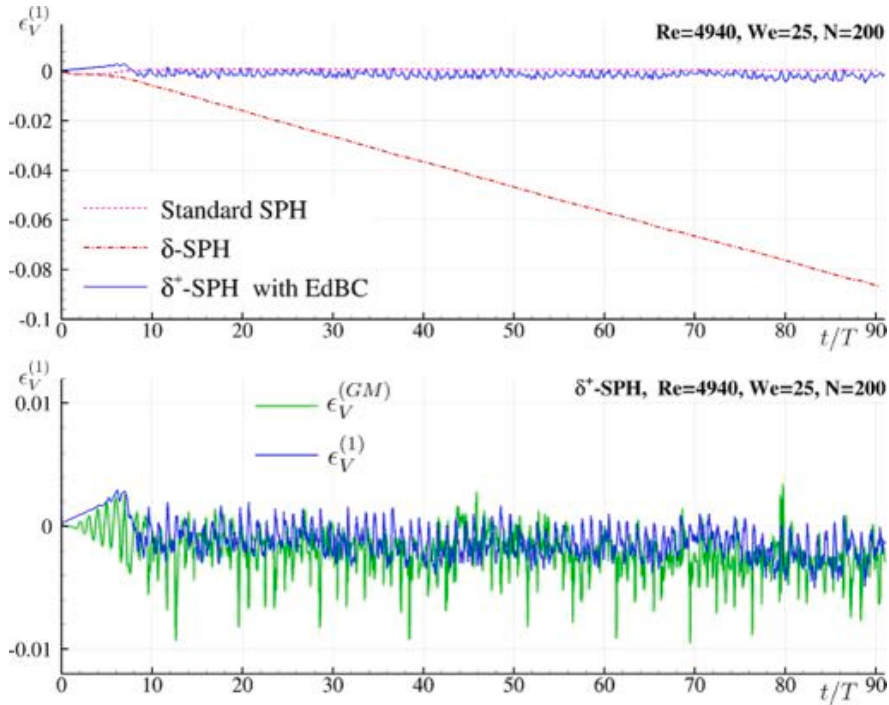
Fig. 17. Time histories of volume error. Top: Comparison between the three SPH models. Bottom: Comparison between the run-time procedure, $\epsilon_V^{(1)}$, and the graphical method ϵ_V^{GM} (see Section 3) for the δ^+-SPH model.
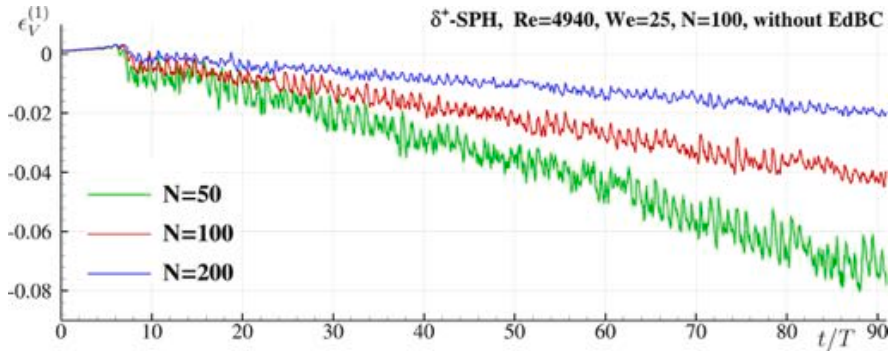

Fig. 18. Time histories of volume error. The δ^+-SPH model is used without EdBC for three different spatial resolutions N=50, 100, 200.
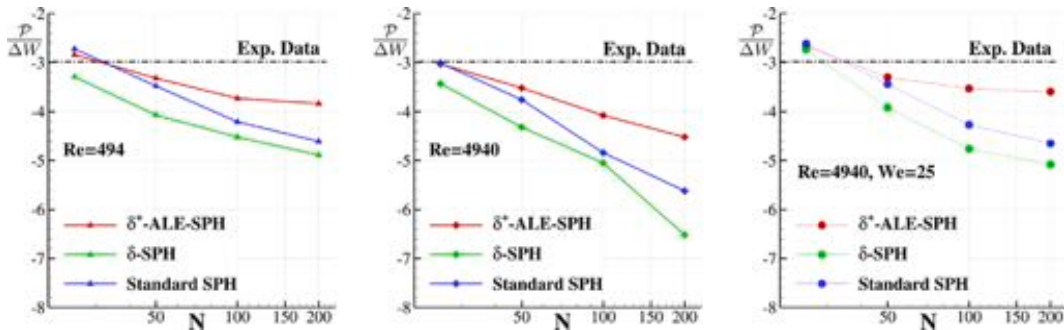

Fig. 19. Sloshing dissipated energy for each oscillation period for three SPH models varying the simulating parameters. Left: Re = 494, middle: Re = 4940, right: Re = 4940 and We = 25. The horizontal dash-dotted line represents the experimental value from [54].
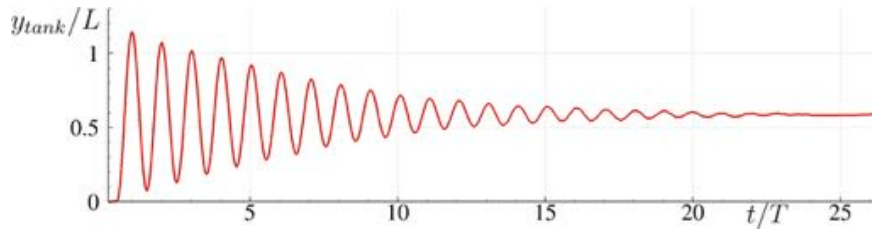
Fig. 20. Time histories of the vertical displacement of the tank.
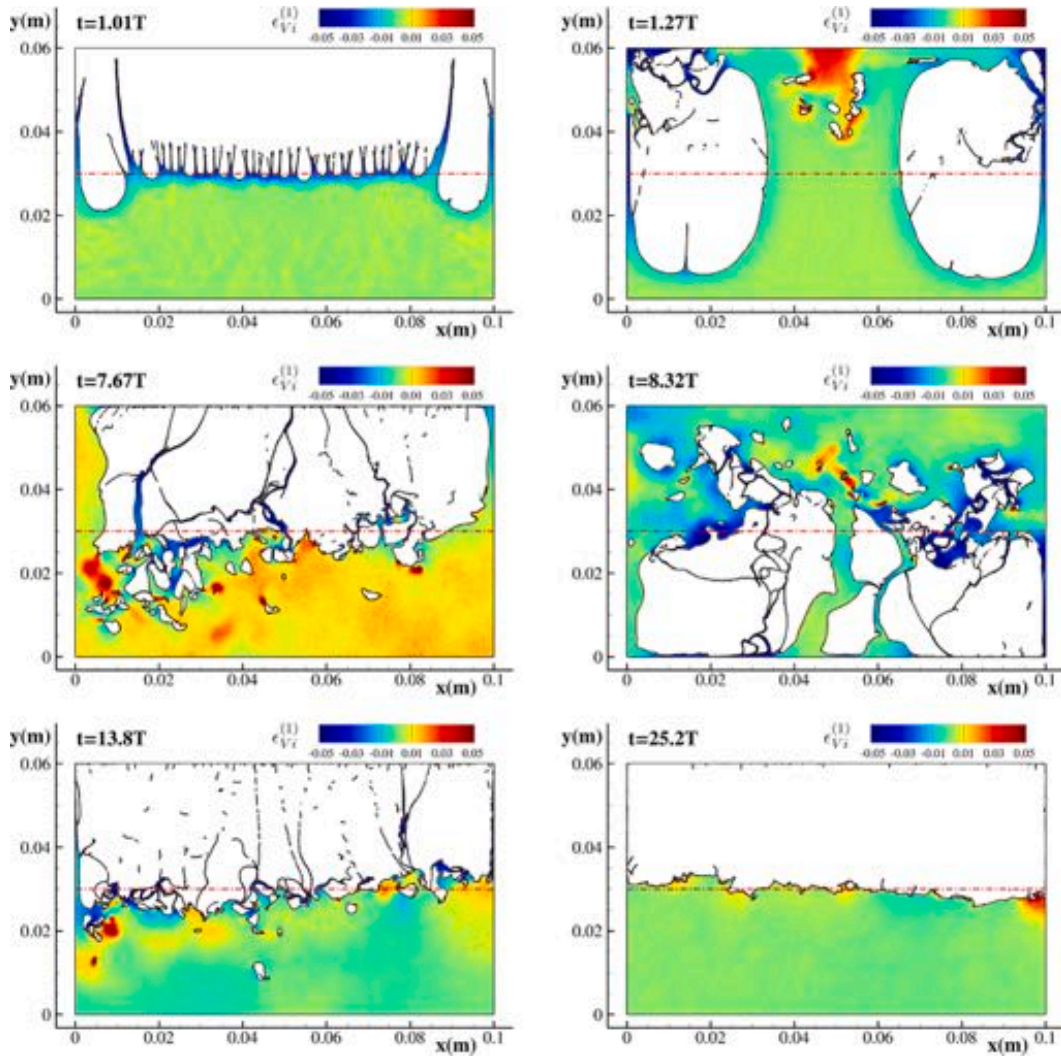
Fig. 21. Heave sloshing in decay motion: contour plot of the local error on volume for the δ^+-ALE-SPH model without surface tension. Spatial resolution $N = 800$. The dash-dotted line refers to the initial filling height H. The video of the simulation is available at Link Video N1.

Fig. 26 shows the δ^+-ALE-SPH solution. Even if the main feature of the flow commented in the previous section for $We = \infty$ is also here well visible, the effects of the surface tension of the flow evolution are evident.

Regarding the sloshing dissipation, the experimental data have been reported in [58]. Fig. 27 shows the sloshing dissipation made dimensionless using the energy potential gap $\Delta E_P = M_l \, g \, 2A = 201$ mJ, instead of the reference kinetic energy $\Delta E = 489$ mJ reported in Table 3.
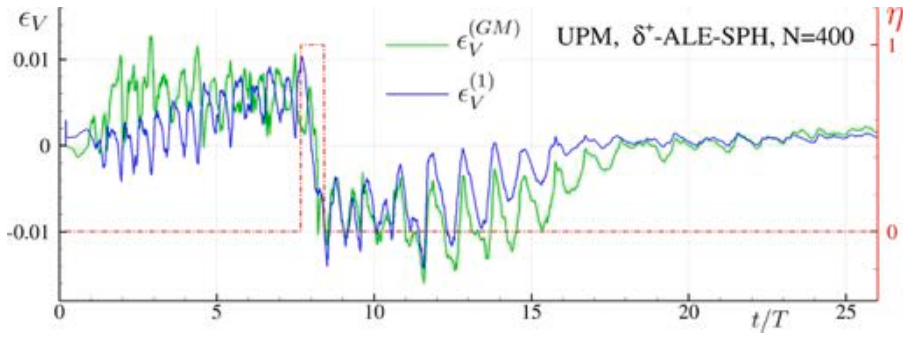
Fig. 22. Time histories of volume error. Comparison between the run-time procedure, $\epsilon_V^{(1)}$, and the graphical method ϵ_V^{GM} (see Section 3).
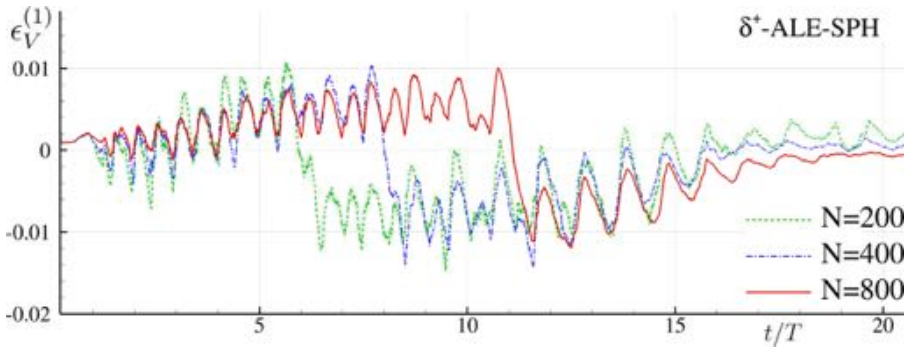
Fig. 23. Time histories of volume error for three different spatial resolutions $N = 200, 400$ and 800.
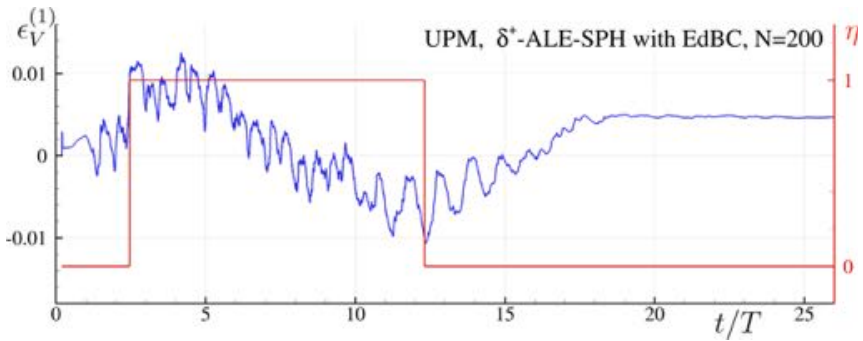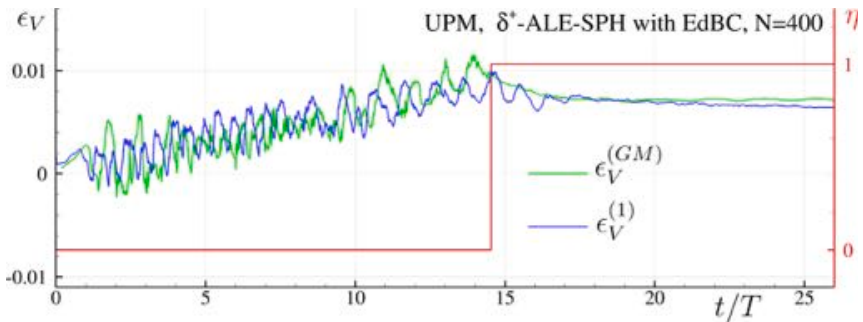

Fig. 24. Test-case #2 with surface tension: time histories of volume error with the δ^+-ALE-SPH model. Spatial resolution N=200. For the latter the comparison between the run-time procedure, $\epsilon_V^{(1)}$, and the graphical method ϵ_V^{GM} (see Section 3) is also reported.

Fig. 25. Test-case #2 with surface tension: time histories of volume error with the δ^+-ALE-SPH model. Spatial resolution N=400. For the latter the comparison between the run-time procedure, $\epsilon_V^{(1)}$, and the graphical method ϵ_V^{GM} (see Section 3) is also reported.
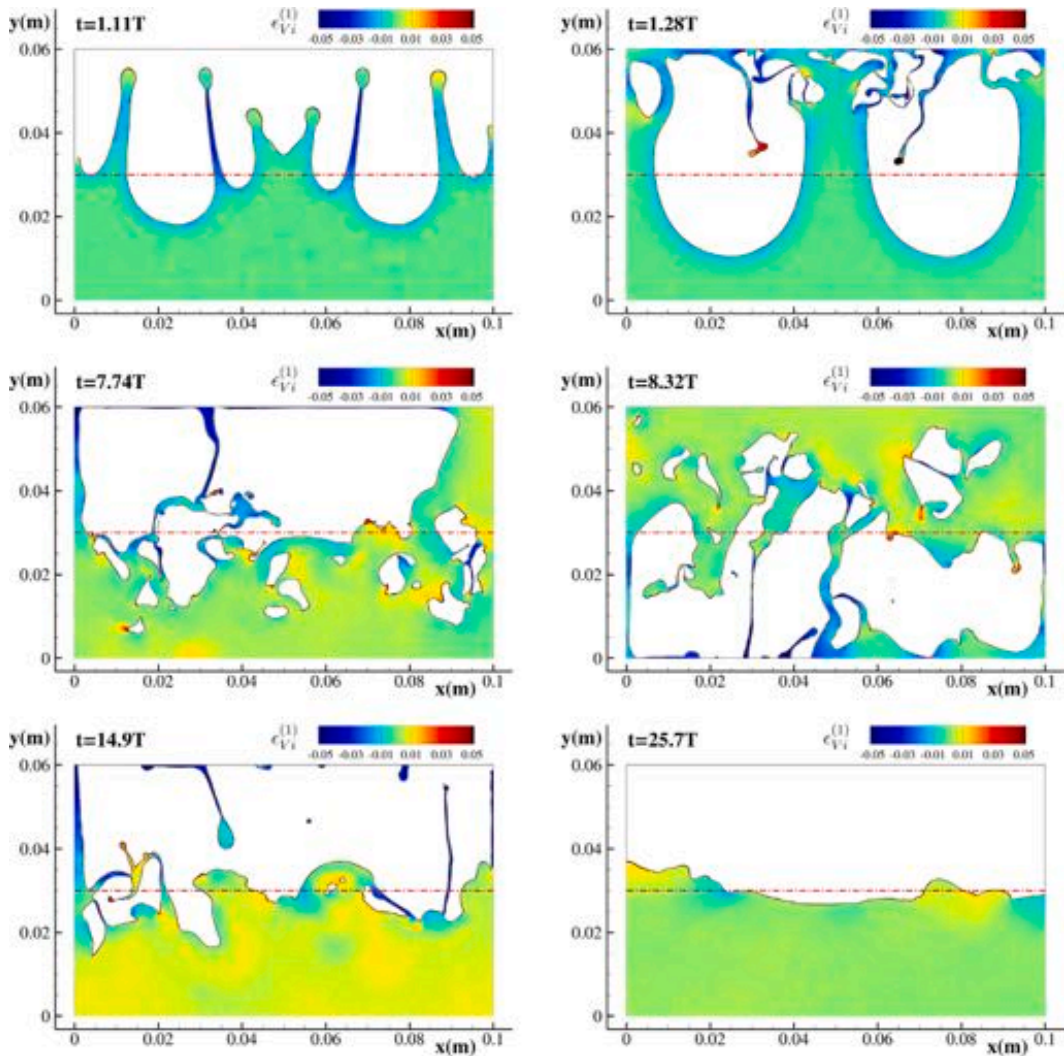
Fig. 26. Heave sloshing in decay motion: contour plot of the local error on volume for the δ^+-ALE-SPH model with surface tension. The dash-dotted line refers to the initial filling height H. Spatial resolution $N = 800$. The video of the simulation is available at Link Video N2.

Several numerical simulations were performed for different spatial resolutions in the range $N \in [50 : 800]$. For the case with $We = \infty$, no-slip boundary conditions were enforced and the δ^+-ALE-SPH solutions are compared with the ones in [59] where free-slip are used. This plot displays the role of the boundary layer that is more important than the surface tension. The underestimation of E_{diss} is linked to the 2D framework as shown in [23] where 3D simulations are considered. As remarked in the [23,58,59], due to the chaotic nature of the flow, the slosh dissipation reported in Fig. 27 is obtained by averaging the results of 10 different simulations.

The averaging was performed for the four different spatial resolutions ($N = 50, 100, 200$ and 400), indeed, the CPU costs for resolution $N = 800$ are too large to perform ten runs even for a 2D framework (see Table 6). The limitation is not mainly linked to the number of particles, which is about two million for $N = 800$, but to the fact that more than 1.5 million time iterations are required.

5.3. Intermediate water — periodic sway sloshing

In this section the periodic sway sloshing INM1 and INM2 described in Section 4.3 is analysed with δ^+-ALE-SPH simulations. Being the test-case INM2 quite energetic we performed the analysis on the volume error both in 2D and in 3D framework.

5.3.1. Test-case INM1

The analysis begins with the test case INM1 where only 2D simulations were considered, indeed, the comparisons of the 2D simulations with the experimental data are quite good in terms of free-surface motions as described in [60,61].
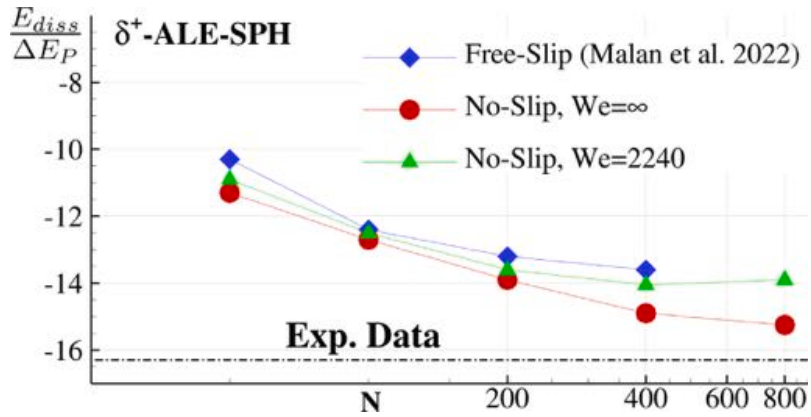
Fig. 27. Test-case #3: Sloshing dissipated energy of the δ^+-ALE-SPH model varying the spatial resolution and considering free-slip and no-slip solid boundary conditions. For the latter, the simulations were performed also with and without surface tension.
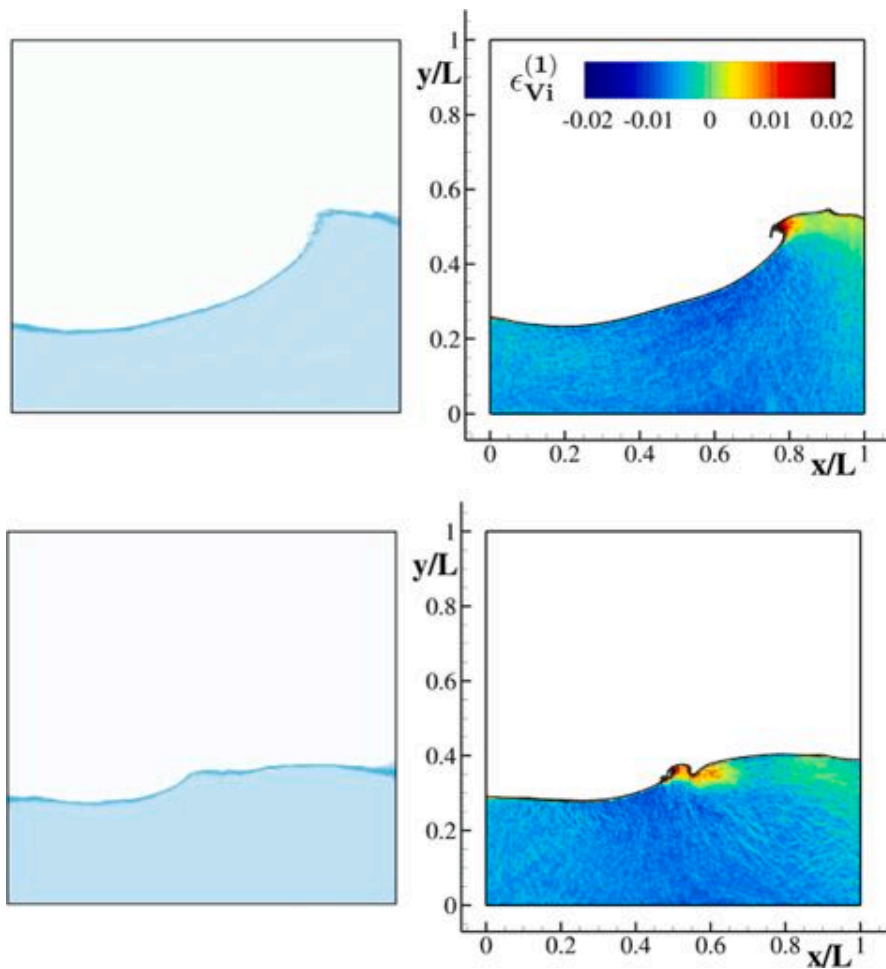

Fig. 28. INM1: experimental snapshots (left) and 2D δ^+-ALE-SPH results (right).

In the latter works, it is shown that the amplitude A=5 cm and the oscillation period $T = 1.1$ seconds of this test-case induce a tripling-period regime characterized by the development of a wave breaking near one of the side walls every three periods of oscillations. As already remarked above, the breaking waves involve fluid–fluid impacts, which can lead to volume errors. However,
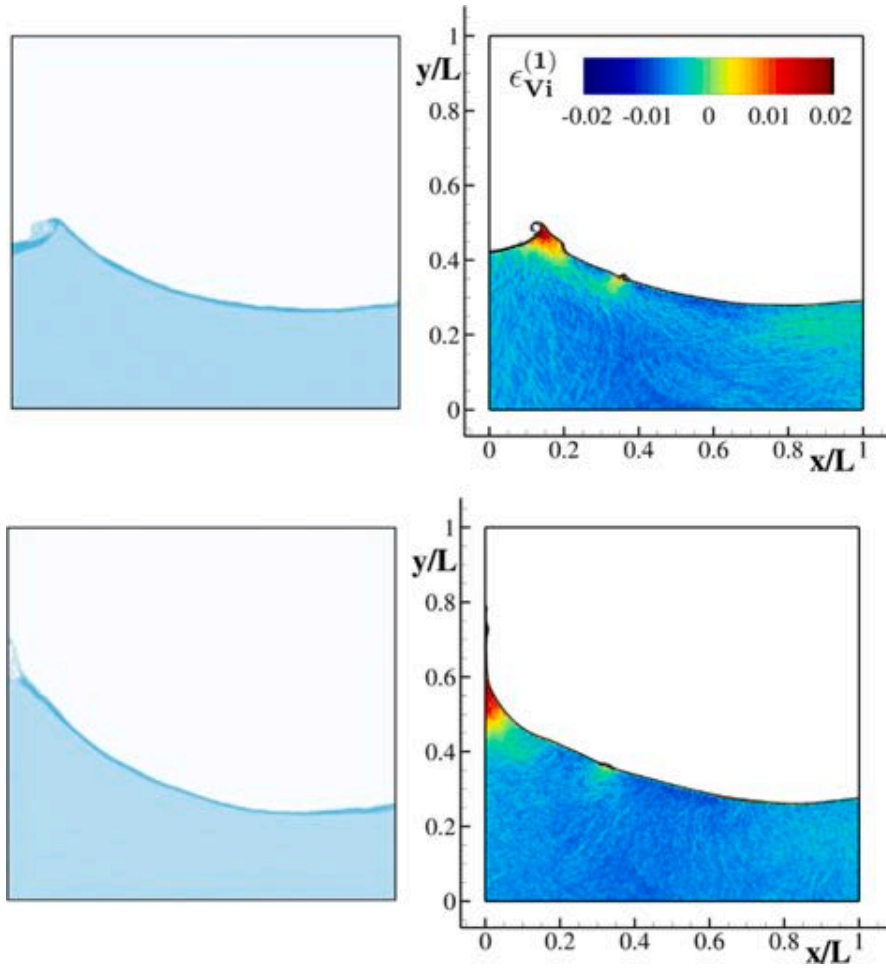
Fig. 29. INM1: experimental snapshots (left) and 2D δ^+-ALE-SPH results (right).

for the INM1 case such phenomena are weakly energetic, therefore, small volume errors are expected at each sloshing cycle. On the other hand, the test-case last for 270 periods and for this long-time evolution errors can accumulate significantly.

Figs. 28 and 29 depict the comparison between experimental pictures (left column) and δ^+-ALE-SPH simulation (right column). In the latter, the particles are coloured with the local error $\epsilon_{Vi}^{(1)}$, and as expected, these errors are just localized in a small portion of the fluid domain. The volume errors increase inside the breaking wave region and on the jets running up the vertical walls after the wave impacts.

The time behaviour recorded for volume error $\epsilon_V^{(1)}$ is reported in Fig. 30 where it is possible to see that two switches of η are necessary to maintain the error bounded within the 1% threshold. The first switch is activated during the initial sloshing stage which is characterized by a more violent fluid motion with respect to the final periodic regime. Since the 272 oscillation periods are simulated, the particle configurations are saved just for the last 40 periods, hence, the volume error $\epsilon_V^{(GM)}$, evaluated with the graphical method, was performed only for those last periods. The error $\epsilon_V^{(GM)}$ is also reported in Fig. 30 showing again a good matching with $\epsilon_V^{(1)}$.

5.3.2. Test-case INM2: 2D simulation

Test INM2 is characterized by an amplitude of the tank motion $A = 10$ cm with an oscillation period of $T = 1$ second. It follows that the sloshing flow is much more violent in the INM2 test-case than the previous one. As commented in [60,62,63] in these conditions an asymmetric behaviour takes place since water impacts only on one side of the tank for several oscillations and then the behaviour reverses on the other side.

Fig. 31 depicts the time histories of volume error of δ^+-ALE-SPH results. It is possible to observe that in this test-case 15 switches of the η parameter are needed to control the volume error. For this reason, the test-case INM2 is the most demanding benchmark among the four discussed in this work. The sign of $\epsilon_V^{(1)}$ changes frequently due to the strong fragmentation of the flow.
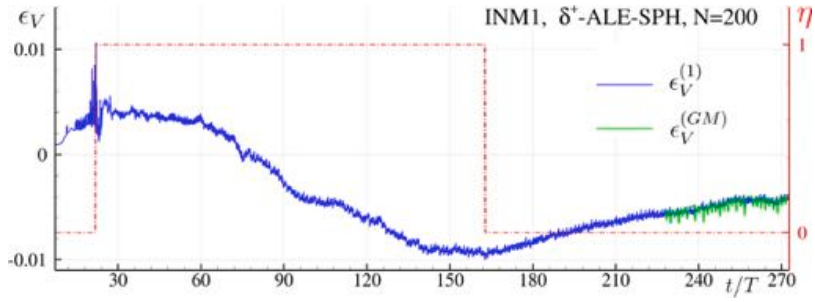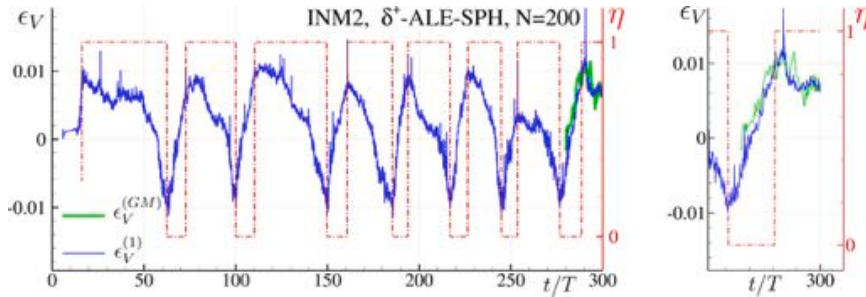
Fig. 30. Time histories of volume error. Comparison between the run-time procedure, $\epsilon_V^{(1)}$, and the graphical method ϵ_V^{GM} (see Section 3).

Fig. 31. Time histories of volume error. Comparison between the run-time procedure, $\epsilon_V^{(1)}$, and the graphical method ϵ_V^{GM} (see Section 3).

The volume error measured by the graphical method, ϵ_V^{GM}, is also plotted in Fig. 31. Because of the complexity of the flow, the ϵ_V^{GM} trend is characterized by intense high-frequency variations. Through a filter operation on ϵ_V^{GM}, it is possible to reach a fair agreement with $\epsilon_V^{(1)}$. Fig. 32 shows the fields of the local volume errors of the δ^+-ALE-SPH simulation for four different time instants during the last oscillation periods. During this time interval the water impacts only on the right vertical side. These impacts are quite violent generating a large fragmentation of the free-surface, with the formation of jets and drops. Because of these phenomena, the local volume errors are higher than the ones depicted for the INM1 test-case. Comparing the δ^+-ALE-SPH results with the experimental data no-negligible differences in the free-surface configurations are found, indeed, the 3D effects are quite relevant. Therefore, the comparison with the experimental data is performed only for the 3D simulations (see next Section 5.3.3).

5.3.3. Test-case INM2: 3D simulation

To demonstrate the effectiveness of the volume controlling techniques for 3D SPH simulations, in this subsection, the INM2 sloshing test is numerically simulated in three dimensions. The length, height and thickness of the tank are 1 m, 1 m and 0.1 m, respectively, as used in the experiment. The particle resolution adopted in the simulation is $H/\Delta x = 40$ where the initial water depth is $H = 0.35$ m.

The time evolution of total volume error $\epsilon_V^{(1)}$ in 3D SPH simulation is presented in Fig. 33. It can be easily observed that $\epsilon_V^{(1)}$ fluctuates between -1% and 1% as in the 2D simulations and it proves that the proposed techniques on the control of the volume can effectively preserve the total volume error even for long-time and 3D violent free-surface flows. In the 3D SPH simulations, when $\epsilon_V^{(1)}$ becomes greater than 1%, δ-ALE-SPH (*i.e.* $\eta = 1$) is used but the EdBC correction is switched off. These conditions lead to a decrement of $\epsilon_V^{(1)}$. When $\epsilon_V^{(1)}$ becomes less than -1%, δ^+-SPH (*i.e.* $\eta = 0$) is used and the EdBC correction is switched on, resulting in the increment of $\epsilon_V^{(1)}$. In this case, the number of switches in η needed to control the volume is seven in ninety oscillations against fifteen in 300 oscillations necessary in the 2D simulation, hence, in 3D framework the number of switches necessary to control the volume error can be in principle higher than in 2D.

In Figs. 34 and 35, 3D SPH results of INM2 are presented and compared against with experimental snapshots. With respect to the 2D SPH simulations, a better agreement can be found between experimental snapshots and 3D SPH results.

In the SPH results the particles are coloured with volume errors $\epsilon_{V\,i}^{(1)}$ which appear confined within few percentage, hence, much smaller than the results presented for the 2D simulation. This is just due to the time instants selected for which total volume error $\epsilon_V^{(1)}$ is crossing the zero level as depicted in Fig. 33.
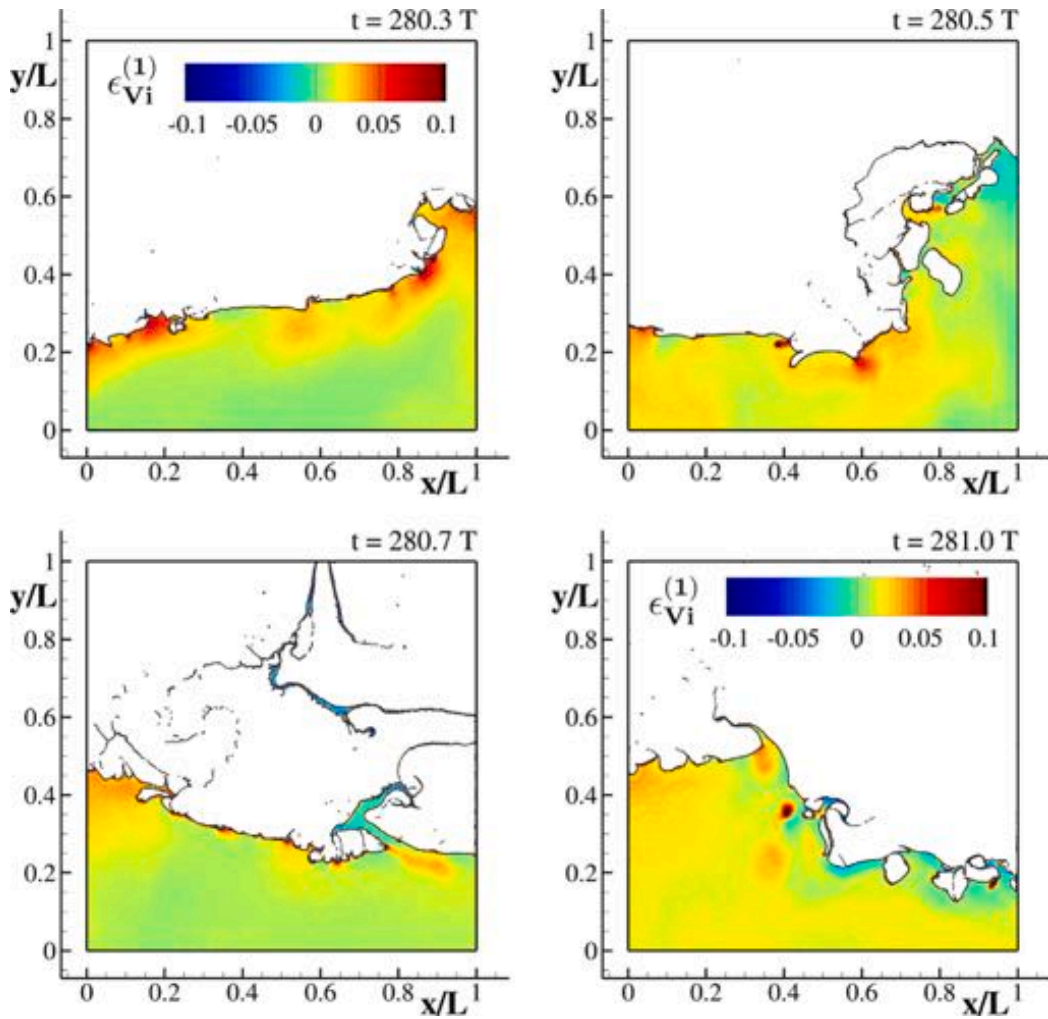
Fig. 32. INM2: volume errors fields in 2D δ^+-ALE-SPH results at the four time instants.
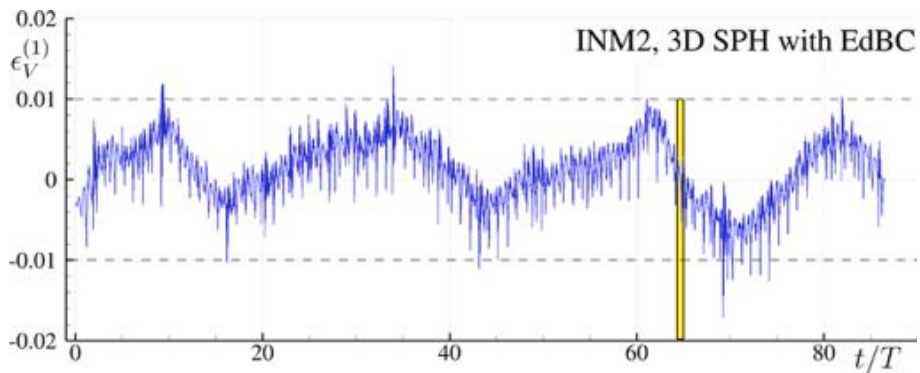

Fig. 33. INM2 — time evolution of volume error ϵ_V using 3D SPH with EdBC. Yellow vertical bar refers to the time interval of the snapshots of Figs. 34 and 35.
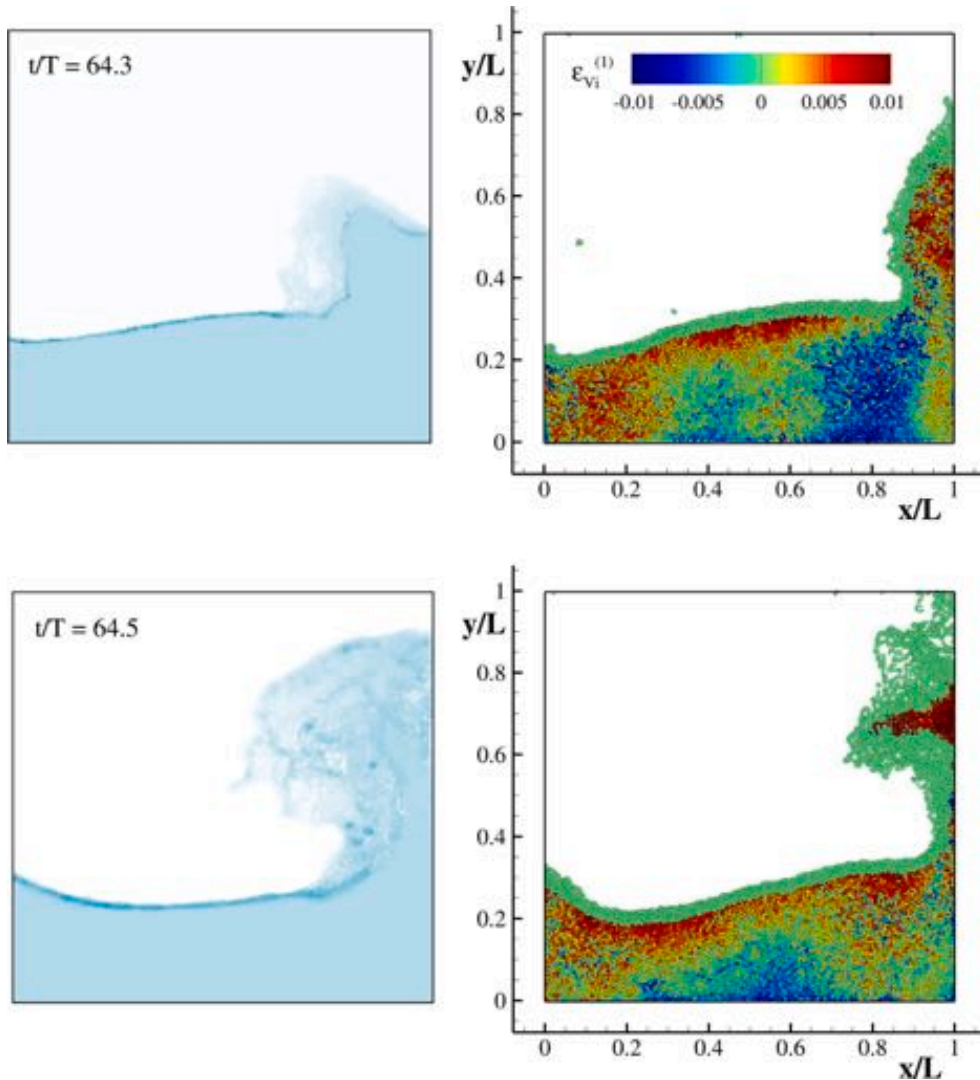
Fig. 34. INM2: experimental snapshots and 3D SPH results with EdBC.

6. Conclusions

In the present work, volume conservation problems encountered in SPH simulations on long-time violent sloshing flows are investigated. All the test-cases considered, validated with experimental data available in the literature, are characterized by high Reynolds numbers.

From a theoretical perspective, it is shown that, when using the standard weakly-compressible SPH method, the total volume of the fluid is always preserved with errors that were always less than 1%. The latter are mainly linked to the time integration of the continuity equation. On the other hand, the solutions obtained with the Standard SPH scheme are affected by a quite disordered particle displacement and high-frequency noise in the pressure field. The last-mentioned induces an extra numerical dissipation when comparing the SPH outputs with experimental data.

To avoid such instability on the pressure field, different SPH variants use numerical diffusive corrections in the continuity equation, which however altered the link between the particles' volumes and their positions through the relation between mass and density. As a result, when simulating violent free-surface flows, especially when the free-surface is highly fragmented, volume errors could occur and accumulate in time through secular terms.

Besides the correction with diffusive artificial terms, we also showed that the use of the Particle Shifting Technique has a crucial role in introducing further volume errors.
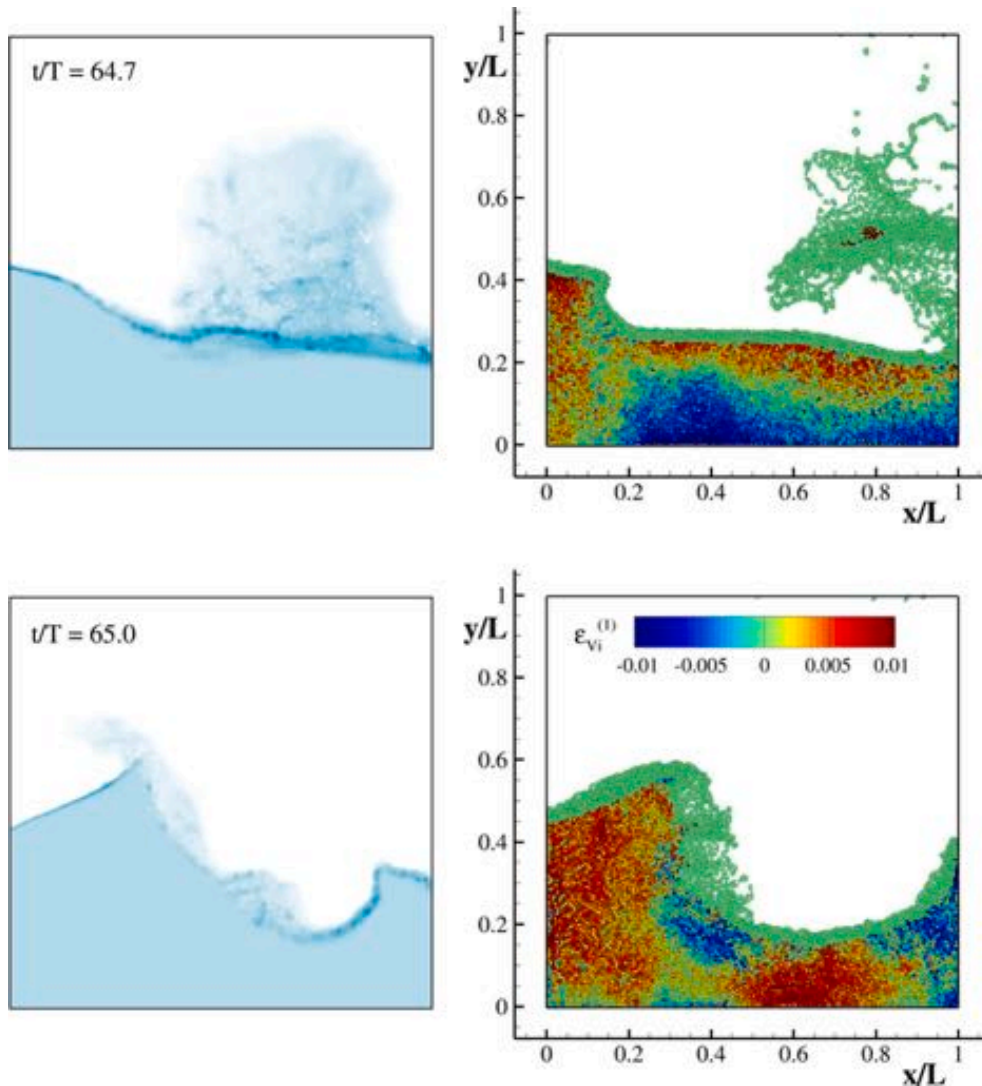
Fig. 35. INM2: experimental snapshots and 3D SPH results with EdBC, continue.

In the present work, two numerical techniques for evaluating the geometrical volume occupied by the set of particles are proposed. While the first one uses the SPH kernel function, in the second one a graphical method is employed directly on the time evolution images stored by the code. These techniques can also be extended to other particle-based methods.

In addition, numerical techniques to control the volume variations are proposed. Two main corrections were found to be effective: (i) a direct enforcement of dynamic boundary conditions on thin jets and drops, (ii) a switch of the parameter η in the SPH equations. In particular, the η parameter allows or blocks the temporal variation of the particle masses. Indeed, what we found is that volume errors accumulate with different signs when particle masses are constant or not in time.

Four different benchmark cases are proposed with the aim to show the characteristics of the volume conservation problem and to test five different SPH schemes. The effect of the fluid viscosity and the surface tension on the volume errors are also investigated. More in detail, it was found that the surface tension drastically inhibits the fragmentation of the flow by reducing the accumulation of volume error.

Both 2D and 3D simulations are executed and they show the effectiveness of the numerical techniques for controlling the total volume. The present work has the goal to provide a framework for the investigations of the volume conservation issues in particle-based numerical models. In future works, a focused theoretical investigation of volume conservation issues will be conducted.

Declaration of competing interest

The authors declare that they have no known competing financial interests or personal relationships that could have appeared to influence the work reported in this paper.

Data availability

Data will be made available on request.

Appendix. Other techniques to evaluate the volume error

Second method run-time

This third method, similarly to the first one, exploits the property that the kernel summation: $\Gamma_i = \sum_i W_{ij} V_j$ has to be close to 1 for all the particles which are not belong to free-surface region $\mathscr{S}_F$. Likewise, because of the kernel truncation for the particle in $\mathscr{S}_F$, Γ_i is assumed to be equal to 1. Taking into account that with the above hypothesis Γ_i is always close to 1 it follows that: $1/\Gamma_i \simeq 2 - \Gamma_i$. Following again [52], the error ϵ_V can be approximated as:

$$\epsilon_V \simeq \frac{\sum_i \frac{V_{i0}}{\Gamma_i}}{V_0} - 1 = \frac{V_{i0} \sum_i (2 - \Gamma_i)}{V_0} - 1 = 1 - \frac{\sum_i \Gamma_i}{N_{part}} = 1 - \overline{\Gamma} \tag{A.1}$$

Therefore, the second approximation for the error ϵ_V is given as:

$$\epsilon_V^{(2)} = (1 - \overline{\Gamma}), \quad \overline{\Gamma} = \frac{\sum_i \Gamma_i}{N_{part}}, \quad \Gamma_i = \begin{cases} \sum_j W_{ij} V_j & \forall i \notin \mathscr{S}_F \\ 1 & \forall i \in \mathscr{S}_F \end{cases} \tag{A.2}$$

For all the simulations and for all the SPH models there are no sensitive differences between $\epsilon_V^{(2)}$ and $\epsilon_V^{(1)}$ (see Eq. (12)).

Third method run-time

The minimum eigenvalue λ_i is close to 1 when the particles are regularly distributed and the number of particles within the kernel support is large enough. Furthermore, in such a condition the sum of the minimum and maximum eigenvalues is in first approximation equal to the $2\Gamma_i$ while the differences tend to be zero. With the above observations, it is possible to define the third approximation for the error ϵ_V:

$$\epsilon_V^{(3)} = (1 - \overline{\lambda}), \quad \overline{\lambda} = \frac{\sum_i \lambda_i}{N_{part}}, \quad \lambda_i = \begin{cases} \text{minimum eigenvalue of } \mathbb{L}_i & \forall i \notin \mathscr{S}_F \\ 1 & \forall i \in \mathscr{S}_F \end{cases} \tag{A.3}$$

The differences with respect to $\epsilon_V^{(2)}$ is that numerically λ_i is more sensitive to variation of the particle displacements with respect to Γ_i.

In all the simulations $\epsilon_V^{(3)}$ and $\epsilon_V^{(1)}$ are quite close when using δ^+-ALE-SPH method. Conversely, in both the Standard SPH and the δ-SPH variants $\epsilon_V^{(3)}$ provides results that are different from the ones obtained with the procedure $\epsilon_V^{(1)}$. This is linked to the particle distributions which are not uniform enough for those two latter methods as commented in Section 5.1.

References

[1] D. Violeau, B.D. Rogers, Smoothed particle hydrodynamics (SPH) for free-surface flows: past, present and future, J. Hydraul. Res. 54 (2016) 1–26.

[2] M.S. Shadloo, G. Oger, D. Le Touzé, Smoothed particle hydrodynamics method for fluid flows, towards industrial applications: Motivations, current state, and challenges, Comput. & Fluids 136 (2016) 11–34.

[3] X.S. Guan, P.N. Sun, H.G. Lyu, N.N. Liu, Y.X. Peng, X.T. Huang, Y. Xu, Research progress of SPH simulations for complex multiphase flows in ocean engineering, Energies 15 (9000) (2022).

[4] H. Gotoh, A. Khayyer, On the state-of-the-art of particle methods for coastal and ocean engineering, Coastal Eng. J. 60 (2018) 79–103.

[5] M. Luo, A. Khayyer, P. Lin, Particle methods in ocean and coastal engineering, Appl. Ocean Res. 114 (2021) 102734.

[6] M. Liu, G. Liu, Smoothed particle hydrodynamics (SPH): an overview and recent developments, Arch. Comput. Methods Eng. 17 (2010) 25–76.

[7] D. Violeau, Fluid Mechanics and the SPH Method, Oxford University Press, 2012.

[8] J.J. Monaghan, Smoothed particle hydrodynamics, Rep. Progr. Phys. 68 (2005) 1703–1759.

[9] J.M. Domínguez, A.J. Crespo, D. Valdez-Balderas, B.D. Rogers, M. Gómez-Gesteira, New multi-gpu implementation for smoothed particle hydrodynamics on heterogeneous clusters, Comput. Phys. Comm. 184 (2013) 1848–1860.

[10] G. Oger, D. Le Touzé, D. Guibert, M. De Leffe, J. Biddiscombe, J. Soumagne, J.G. Piccinali, On distributed memory mpi-based parallelization of SPH codes in massive hpc context, Comput. Phys. Comm. 200 (2016) 1–14.

[11] L. Zhan, C. Peng, B. Zhang, W. Wu, A stabilized tl–wc SPH approach with gpu acceleration for three-dimensional fluid–structure interaction, J. Fluids Struct. 86 (2019) 329–353.

[12] G. Oger, A. Vergnaud, B. Bouscasse, J. Ohana, M. Abu Zarim, M. De Leffe, A. Bannier, L. Chiron, Y. Jus, M. Garnier, et al., Simulations of helicopter ditching using smoothed particle hydrodynamics, J. Hydrodyn. 32 (2020) 653–663.

[13] H.G. Lyu, P.N. Sun, X.T. Huang, Y.X. Peng, N.N. Liu, X. Zhang, Y. Xu, A. Zhang, Sphydro: Promoting smoothed particle hydrodynamics method toward extensive applications in ocean engineering, Phys. Fluids 35 (2023) 017116.

[14] P. Nair, G. Tomar, Volume conservation issues in incompressible smoothed particle hydrodynamics, J. Comput. Phys. 297 (2015) 689–699.

[15] Q. Gui, P. Dong, S. Shao, Numerical study of ppe source term errors in the incompressible sph models, Internat. J. Numer. Methods Fluids 77 (2015) 358–379.

[16] X. Zheng, Y. You, Q. Ma, A. Khayyer, S. Shao, A comparative study on violent sloshing with complex baffles using the isph method, Appl. Sci. 8 (904) (2018).

[17] P. Suchde, C. Leithäuser, J. Kuhnert, S. Bordas, Volume and mass conservation in lagrangian meshfree methods, 2023, arXiv preprint arXiv:2303.13410.

[18] J. Monaghan, Smoothed particle hydrodynamics, Ann. Rev. Astron. Astrophys. 30 (1992) 543–574.

[19] J. Monaghan, Simulating free surface flows with SPH, J. Comp. Phys. 110 (1994) 39–406.

[20] A. Colagrossi, M. Landrini, Numerical simulation of interfacial flows by smoothed particle hydrodynamics, J. Comp. Phys. 191 (2003) 448–475.

[21] J. Vila, On particle weighted methods and smooth particle hydrodynamics, Math. Models Methods Appl. Sci. 9 (1999) 161–209.

[22] B. Ben Moussa, J. Vila, Convergence of SPH method for scalar nonlinear conservation laws, SIAM J. Numer. Anal. 37 (3) (2000) 863–887.

[23] J. Michel, D. Durante, A. Colagrossi, S. Marrone, Energy dissipation in violent three-dimensional sloshing flows induced by high-frequency vertical accelerations, Phys. Fluids 34 (2022) 102114.

[24] M. Antuono, A. Colagrossi, S. Marrone, Numerical diffusive terms in weakly-compressible SPH schemes, Comput. Phys. Comm. 183 (2012) 2570–2580.

[25] M. Antuono, S. Marrone, A. Colagrossi, B. Bouscasse, Energy balance in the δ-SPH scheme, Comput. Methods Appl. Mech. Engrg. 289 (2015).

[26] R.M. Nestor, M. Basa, M. Lastiwka, N.J. Quinlan, Extension of the finite volume particle method to viscous flow, J. Comput. Phys. 228 (2009) 1733–1749.

[27] S. Lind, R. Xu, P. Stansby, B. Rogers, Incompressible smoothed particle hydrodynamics for free-surface flows: A generalised diffusion-based algorithm for stability and validations for impulsive flows and propagating waves, J. Comput. Phys. 231 (2012) 1499–1523.

[28] A. Khayyer, H. Gotoh, Y. Shimizu, Comparative study on accuracy and conservation properties of two particle regularization schemes and proposal of an optimized particle shifting scheme in ISPH context, J. Comput. Phys. 332 (2017) 236–256.

[29] P. Sun, A. Colagrossi, S. Marrone, M. Antuono, A.M. Zhang, A consistent approach to particle shifting in the δ-plus-SPH model, Comput. Methods Appl. Mech. Engrg. 348 (2019) 912–934.

[30] A. Khayyer, Y. Shimizu, T. Gotoh, H. Gotoh, Enhanced resolution of the continuity equation in explicit weakly compressible SPH simulations of incompressible free-surface fluid flows, Appl. Math. Model. 116 (2023) 84–121.

[31] H.G. Lyu, P.N. Sun, Further enhancement of the particle shifting technique: Towards better volume conservation and particle distribution in SPH simulations of violent free-surface flows, Appl. Math. Model. 101 (2022) 214–238.

[32] T. Gao, L. Fu, A new particle shifting technique for SPH methods based on voronoi diagram and volume compensation, Comput. Methods Appl. Mech. Engrg. 404 (2023) 115788.

[33] H.S. Yoo, Y.B. Jo, J.W. Kim, E.S. Kim, T.S. Choi, A simple eulerian–lagrangian weakly compressible smoothed particle hydrodynamics method for fluid flow and heat transfer, Internat. J. Numer. Methods Engrg. 124 (2023) 928–958.

[34] M. Antuono, P. Sun, S. Marrone, A. Colagrossi, The δ-ALE-SPH model: An arbitrary lagrangian-eulerian framework for the δ-SPH model with particle shifting technique, Comput. & Fluids 216 (2021b) 104806.

[35] H. Wendland, Piecewise polynomial, positive definite and compactly supported radial functions of minimal degree, Adv. Comput. Math. 4 (1995) 389–396.

[36] A. Colagrossi, D. Durante, J. Bonet-Avalos, A. Souto-Iglesias, Discussion of Stokes' hypothesis through the smoothed particle hydrodynamics model, Phys. Rev. E 96 (2017).

[37] C. Bailly, G. Comte-Bellot, The Dynamics of Isotropic Turbulence, Vol. 17, Springer International Publishing, 2015, pp. 9–210.

[38] M. Antuono, S. Marrone, A. Di Mascio, A. Colagrossi, Smoothed particle hydrodynamics method from a large eddy simulation perspective. generalization to a quasi-lagrangian model, Phys. Fluids 33 (2021a) 015102.

[39] E.R. Van Driest, On turbulent flow near a wall, J. Aeronaut. Sci. 23 (1956) 1007–1011.

[40] C. Pilloton, J. Michel, A. Colagrossi, S. Marrone, A numerical investigation on three-dimensional swirling instability in viscous sloshing flows, Appl. Ocean Res. 138 (2023) 103621.

[41] A. Di Mascio, M. Antuono, A. Colagrossi, S. Marrone, Smoothed particle hydrodynamics method from a large eddy simulation perspective, Phys. Fluids 29 (2017) 1–14.

[42] M. Antuono, A. Colagrossi, S. Marrone, D. Molteni, Free-surface flows solved by means of SPH schemes with numerical diffusive terms, Comput. Phys. Comm. 181 (2010) 532–549.

[43] P. Sun, A. Colagrossi, S. Marrone, M. Antuono, A. Zhang, Multi-resolution delta-plus-SPH with tensile instability control: Towards high reynolds number flows, Comput. Phys. Comm. 224 (2018) 63–80.

[44] A. Vergnaud, G. Oger, D. Le Touzé, M. DeLeffe, L. Chiron, C-csf: Accurate, robust and efficient surface tension and contact angle models for single-phase flows using SPH, Comput. Methods Appl. Mech. Engrg. 389 (2022) 114292.

[45] J. Calderon-Sanchez, J. Martinez-Carrascal, L. Gonzalez-Gutierrez, A. Colagrossi, A global analysis of a coupled violent vertical sloshing problem using an SPH methodology, Eng. Appl. Comput. Fluid Mech. 15 (2021) 865–888.

[46] S. Marrone, A. Colagrossi, A. Di Mascio, D. Le Touzé, Prediction of energy losses in water impacts using incompressible and weakly compressible models, J. Fluids Struct. 54 (2015) 802–822.

[47] S. Marrone, A. Colagrossi, A. Di Mascio, D. Le Touzé, Analysis of free-surface flows through energy considerations: Single-phase versus two-phase modeling, Phys. Rev. E 93 (2016) 053113.

[48] J. Monaghan, SPH without a tensile instability, J. Comp. Phys. 159 (2000) 290–311.

[49] P. Sun, A. Colagrossi, S. Marrone, A. Zhang, The δplus-SPH model: Simple procedures for a further improvement of the sph scheme, Comput. Methods Appl. Mech. Engrg. 315 (2017) 25–49.

[50] A. Colagrossi, E. Rossi, S. Marrone, D. Le Touzé, Particle methods for viscous flows: Analogies and differences between the SPH and DVH methods, Commun. Comput. Phys. 20 (2016) 660–688.

[51] S. Marrone, A. Colagrossi, D.L. Touzé, G. Graziani, Fast free-surface detection and level-set function definition in SPH solvers, J. Comput. Phys. 229 (2010) 3652–3663.

[52] Español P., M. Revenga, Smoothed dissipative particle dynamics, Phys. Rev. E 67 (2003) 026705.

[53] A. Colagrossi, B. Bouscasse, M. Antuono, S. Marrone, Particle packing algorithm for SPH schemes, Comput. Phys. Comm. 183 (2012) 1641–1683.

[54] F. Saltari, M. Pizzoli, G. Coppotelli, F. Gambioli, J.E. Cooper, F. Mastroddi, Experimental characterisation of sloshing tank dissipative behaviour in vertical harmonic excitation, J. Fluids Struct. 109 (2022) 103478.

[55] S. Marrone, F. Saltari, J. Michel, F. Mastroddi, SPH modelling of dissipative sloshing flows under violent vertical harmonic excitation, J. Fluids Struct. 119 (2023) 103877.

[56] J. Martinez-Carrascal, L. González-Gutiérrez, Experimental study of the liquid damping effects on a sdof vertical sloshing tank, J. Fluids Struct. 100 (2021) 103172.

[57] S. Marrone, A. Colagrossi, F. Gambioli, L. González-Gutiérrez, Numerical study on the dissipation mechanisms in sloshing flows induced by violent and high-frequency accelerations. I. theoretical formulation and numerical investigation, Phys. Rev. Fluids 6 (2021b) 114801.

[58] S. Marrone, A. Colagrossi, J. Calderon-Sanchez, J. Martinez-Carrascal, Numerical study on the dissipation mechanisms in sloshing flows induced by violent and high-frequency accelerations. II. comparison against experimental data, Phys. Rev. Fluids 6 (2021a) 114802.

[59] L.C. Malan, C. Pilloton, A. Colagrossi, A.G. Malan, Numerical calculation of slosh dissipation, Appl. Sci. 12 (12390) (2022).

[60] A. Colagrossi, A Meshless Lagrangian Method for Free-Surface and Interface Flows with Fragmentation (Ph.D. thesis), Università di Roma La Sapienza, 2005.

[61] C. Lugni, G. Colicchio, A. Colagrossi, Investigation of sloshing phenomena near the critical filling depth through the hilbert-huang transformation, in: Proc. 9th Numerical Towing Tank Symposium (NuTTS'06) Le Croisic, France, 2006, pp. 89–94.

[62] A. Colagrossi, C. Lugni, M. Greco, O. Faltinsen, Experimental and numerical investigation of 2D sloshing with slamming, in: Proc. 19th Int. Workshop on Water Waves and Floating Bodies, Cortona, Italy, 2004.

[63] O. Faltinsen, A. Timokha, Sloshing, Cambridge University Press, 2009.